

IAEMU: LEARNING GALAXY INTRINSIC ALIGNMENT CORRELATIONS

SNEH PANDYA^{1,2}, YUANYUAN YANG^{1,3}, NICHOLAS VAN ALFEN¹, JONATHAN BLAZEK¹, AND ROBIN WALTERS³


¹Department of Physics, Northeastern University, Boston, MA 02115, USA

³NSF AI Institute for Artificial Intelligence and Fundamental Interactions (IAIFI) and

²Khoury College of Computer Sciences, Northeastern University, Boston, MA 02115, USA

Version 15th May 2025

Abstract

The intrinsic alignments (IA) of galaxies, a significant contaminant in weak lensing analyses, arise from correlations in galaxy shapes driven by gravitational tidal interactions and galaxy formation processes. Understanding IA is therefore essential for deriving accurate cosmological inferences from weak lensing surveys. However, IA modeling relies on a combination of perturbative approaches, which cannot describe nonlinear scales, and expensive simulation-based approaches. In this work, we introduce **IAEmu**, a neural network-based emulator designed to predict the galaxy position-position (ξ), position-orientation (ω), and orientation-orientation (η) correlation functions, and their associated uncertainties, using halo occupation distribution (HOD)-based mock galaxy catalogs. Compared to the simulated catalogs, **IAEmu** exhibits an approximately 3% average error for ξ and 5% for ω , while capturing the stochasticity in η , avoiding overfitting this inherently noisier statistic. Importantly, the emulator also provides aleatoric and epistemic uncertainties, which when analyzed jointly, can help identify regions in parameter space where **IAEmu**'s predictions may be less reliable. Furthermore, we demonstrate the model's generalization to a non-HOD based signal by fitting alignment parameters from the IllustrisTNG hydrodynamical simulations. Since **IAEmu** is a fully differentiable neural network, it enables approximately a 10,000 \times speed-up in mapping HOD parameters to correlation functions when deployed on a GPU, compared to conventional CPU resources. This substantial acceleration also facilitates solving inverse problems more efficiently by supporting gradient-based sampling algorithms. As such, **IAEmu** offers an efficient and accurate surrogate model for halo-based galaxy bias and IA modeling with the potential to significantly expedite model validation in Stage IV weak lensing surveys. 

Keywords: Weak Gravitational Lensing, Intrinsic Alignment, Machine Learning

1. INTRODUCTION

Weak lensing, a subtle yet rich effect that maps the distribution of dark matter and measures cosmic structure growth, is a key cosmological probe for the Legacy Survey of Space and Time (LSST, Ivezić et al. (2019)) of the Vera C. Rubin Observatory, as well as for the *Roman* (Akeson et al. 2019) and *Euclid* (Scaramella et al. 2022) missions. These next-generation surveys will be incredibly powerful, achieving sub-percent levels of statistical precision. The intrinsic alignment (IA) of galaxies, a result of their interactions with large-scale structure and other galaxies, can contaminate weak lensing measurements, necessitating accurate and efficient IA modeling in preparation for future analyses (e.g. Troxel & Ishak 2015; Krause et al. 2016; Blazek et al. 2019; Fortuna et al. 2021; Hoffmann et al. 2022; Secco et al. 2022; Campos et al. 2023; Samuroff et al. 2024; Paopiamsap et al. 2024).

Intrinsic alignment (IA) modeling has traditionally relied on analytic approaches, such as perturbation theory (e.g. Hirata & Seljak 2004; Bridle & King 2007; Blazek et al. 2015, 2019; Vlah et al. 2020, 2021; Maion et al. 2023; Bakx et al. 2023; Chen & Kokron 2023). However,

these analytic models often struggle to accurately capture nonlinear effects. In cosmology, simulation-based approaches that account for both gravitational and baryonic effects, spanning scales from sub-parsec to giga-parsec, have provided profound insights into cosmological evolution (e.g. Villaescusa-Navarro et al. 2021; Nelson et al. 2021; Pillepich et al. 2018; Delgado et al. 2023). These methods have the potential to better capture IA effects compared to purely analytic models. Magneto-hydrodynamic simulations, often referred to as “hydro” simulations, incorporate baryonic effects but exhibit significant variance in their predictions depending on the simulation suite and the sub-grid physics models employed at sub-parsec scales. This variance includes disagreement on IA effects measured in different simulation suites (e.g. Tenneti et al. 2016; Samuroff et al. 2021). Additionally, these simulations are computationally expensive. Given these challenges, gravity-only N-body simulations, such as *AbacusSummit* (Maksimova et al. 2021) and *Quijote* (Villaescusa-Navarro et al. 2020), provide a cost-effective and general alternative. These simulations avoid the need to specify sub-parsec-scale baryonic physics, but inherently lack galaxy formation and evolution processes. To bridge this gap, various halo occupation

* E-mail: pandya.sne@northeastern.edu

distribution (HOD) models have been employed to populate halos from N-body simulations with galaxies. This approach has been extended to include galaxy populations that exhibit correlated alignments (e.g. Joachimi et al. 2013; Hoffmann et al. 2022; Van Alfen et al. 2024).

Despite its utility, HOD modeling can still be computationally demanding, as it requires the generation of extensive galaxy catalogs from halo catalogs and the application of estimators to extract IA and clustering signals. To reduce computational cost and time associated with IA modeling, surrogate modeling based on existing simulations represents a promising avenue of research. One approach that can offer both precision and efficiency is deep learning (DL), by training neural network (NN) surrogates to accelerate numerical simulations. NNs have seen many different scientific applications, including in cosmology (see Dvorkin et al. (2022) for a review), with the availability of large datasets and powerful GPU-driven computation. They not only provide new insights, but also have the potential to accelerate numerous analyses when deployed on GPUs. The benefits of NN-based surrogate models are not exclusive to forward modeling, as the differentiability of such models can also be exploited in accelerating inverse problems using differentiable sampling techniques.

In this work, we introduce a NN-based approach to emulating HOD simulations that models both galaxy bias and IA statistics, referred to as **IAEmu**. This is the first attempt at directly modeling IA statistics from HOD simulations using NNs. **IAEmu** directly models galaxy position and shape correlations for an HOD simulation, bypassing both the generation of a full galaxy catalog and the simulation step itself. This approach offers a significant speed advantage over traditional HOD-based modeling. Additionally, **IAEmu** successfully models galaxy shape statistics, whose stochasticity is dominated by galaxy shape noise, as discussed in Van Alfen et al. (2024). **IAEmu** successfully captures the mean behavior of these noisier statistics, which would otherwise require multiple realizations of the underlying HOD. It also estimates galaxy shape noise (aleatoric uncertainty) and quantifies its own epistemic uncertainty – reflecting uncertainty in the predicted correlation amplitudes – primarily due to limited training data. **IAEmu**’s uncertainty estimates enable one to assess the reliability of these predictions and further enable error propagation in modeling pipelines that incorporate **IAEmu**. We further show the benefits of accelerated parameter inference (i.e., inverse problems) using gradient-based sampling techniques with **IAEmu**, exploiting the fact that NNs are differentiable models.

Related Work. Several previous works have constructed simulation-based emulators for cosmological statistics, with a focus on matter or galaxy density. Zhai et al. (2019) constructed Gaussian process-based emulators based on the AEMULUS Project’s N-body simulations for nonlinear galaxy clustering. Kwan et al. (2023) similarly used a Gaussian process-based emulator, HOD modeling, and the Mira-Titan Suite of N-body simulations to predict galaxy correlation functions, building on earlier work from the same group (Lawrence et al. 2010). The BACCO simulation project (Aricò et al. 2021a, Aricò et al. 2021b) built NN emulators to include nonlinear and baryonic effects from simulations. These

projects emulate various cosmological statistics from simulations, but do not include IA. Jagvaral et al. (2022), Jagvaral et al. (2024), and Jagvaral et al. (2023b) developed generative models trained on the TNG100 simulation (Nelson et al. 2021) to emulate IA in hydrodynamic simulations, but these models do not emulate statistics. Our work is the first to emulate galaxy-IA correlation statistics using simulated galaxy catalogs.

Paper Organization. This paper is organized as follows. Section 2 provides a background on the HOD simulation and correlation function estimators, as well as the procedure for generating and cleaning the training and test data. Section 3 introduces the **IAEmu** architecture and the process for training **IAEmu**. In Section 3, we also analyze the generalization performance of **IAEmu** on held-out data and characterize the quality of predictions based on the predicted aleatoric and epistemic uncertainty. Finally, in Section 4, we validate the out-of-distribution (OOD) performance of **IAEmu** on a non-HOD-based signal from the TNG300 suite of simulations (Nelson et al. 2015; Pillepich et al. 2017; Springel et al. 2017; Nelson et al. 2017; Naiman et al. 2018; Marinacci et al. 2018) by obtaining a posterior on alignment parameters, which is compared with the HOD-based approach. We summarize our main results in Section 5.

2. DATASET: HALO OCCUPATION DISTRIBUTION

This section outlines the basics of the halo occupation distribution, the estimators used by **halotools** to measure correlations, and the generation of the data on which **IAEmu** was trained.

2.1. HOD Background & Estimators

Given a catalog of dark matter halos, we generate a galaxy catalog using an HOD model. This model consists of several interconnected components: (1) an occupation component, which populates halos with galaxies, (2) a phase space component, which determines the spatial distribution of galaxies within halos, and (3) an alignment component, which models galaxy intrinsic alignments. The **halotools** package constructs these HOD-based galaxy catalogs following this framework. Specifically, it employs the halo model (Cooray & Sheth 2002; Asgari et al. 2023) along with alignment models introduced in Van Alfen et al. (2024), providing a flexible approach for generating mock galaxy catalogs while simultaneously tracking intrinsic alignments. We refer to this extension of **halotools**, which incorporates IA information, as **halotools-IA**. This structure enables the rapid generation of multiple galaxy catalogs using consistent occupation, phase space, and alignment parameters. Depending on the chosen HOD parameters, a given halo may or may not host a central galaxy – the most massive galaxy residing at the halo’s center. Additionally, halos may contain satellite galaxies, which are distributed throughout the halo.

Correlation Estimators. To measure the correlations in these catalogs, **halotools-IA** uses the estimators in Equations (1)-(3) for the position-position (ξ), position-orientation (ω), and orientation-orientation (η) correlations, respectively. The ξ correlation is defined as

$$\xi(r) = \left\langle \frac{n(r)}{\bar{n}(r)} \right\rangle - 1, \quad (1)$$

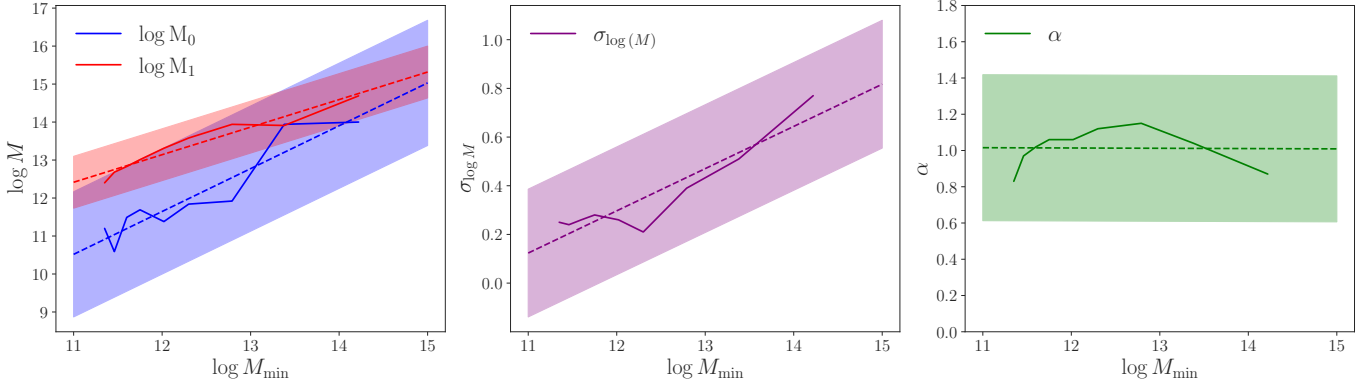


Figure 1. Ranges of HOD parameters used in generating the training data from `halotools-IA`. We generate uniform random values for the four occupation parameters, excluding $\log M_{\min}$. These values are based on a linear relationship with $\log M_{\min}$, serving as a central line. The range for random values extends $4 \cdot \text{RMSE}$ surrounding this line. To clarify the visualization, $\sigma_{\log(M)}$ is displayed separately from other mass variables. Each panel presents published data from Zheng et al. (2007) as a solid line, while the dotted line illustrates the linear fit to $\log M_{\min}$, with the shaded area indicating the range for uniform random value selection for each parameter. Not shown here are the two alignment parameters, μ_{cen} and μ_{sat} , which both vary uniformly on the range $[-1, 1]$ with no relation to these five occupation parameters.

where $n(r)$ is the number of galaxies separated by distance r , and $\bar{n}(r)$ is the expected number of galaxies separated by distance r for a random distribution. This equation is simpler than the Landy-Szalay estimator (Landy & Szalay 1993) and may be suboptimal in some cases (Singh et al. 2017). However, due to the periodic nature of the simulation box, `halotools-IA` can use analytical randoms, mitigating much of this suboptimality. This estimator is also much faster and is sufficient for our HOD models. The ω correlation is defined as

$$\omega(r) = \langle |\hat{e}(\mathbf{x}) \cdot \hat{r}|^2 \rangle - \frac{1}{3}, \quad (2)$$

and quantifies how the orientation of a galaxy at a position \mathbf{x} is aligned with the positions of other galaxies at a distance \mathbf{r} . If ω is positive, the orientation tends to align with the direction to nearby galaxies; if negative, it tends to be perpendicular. Similarly, the η correlation is defined as

$$\eta(r) = \langle |\hat{e}(\mathbf{x}) \cdot \hat{e}(\mathbf{x} + \mathbf{r})|^2 \rangle - \frac{1}{3}, \quad (3)$$

and measures how similarly two galaxies at positions \mathbf{x} and $\mathbf{x} + \mathbf{r}$ are oriented. A positive η indicates that the orientations tend to be aligned, while a negative value means they tend to be perpendicular. For both ω and η , \mathbf{x} is the position vector of a given galaxy, \mathbf{r} is the separation vector between two galaxies, \hat{r} is the unit vector of the separation vector \mathbf{r} , and \hat{e} is the galaxy orientation unit vector. The factor of $1/3$ in these equations accounts for the fact that

$$\frac{1}{4\pi} \int_0^{2\pi} \int_0^\pi \cos^2 \theta \sin \theta d\theta d\phi = \frac{1}{3}, \quad (4)$$

where integrating $\cos^2 \theta$ over a sphere corresponds to the case of random alignments.

Correlation functions are measured for simulated galaxies across 20 bins, evenly spaced in logarithmic scale, between a minimum separation of $0.1 h^{-1} \text{Mpc}$ and a maximum separation of $16 h^{-1} \text{Mpc}$. In future work,

the maximum range of this correlation could be extended. However, for this dataset, we chose this maximum separation because the number of galaxies n increases with r , and the computational cost of measuring correlations scales as $\mathcal{O}(n) \log(n)$. In general, galaxies at $r \leq 1 h^{-1} \text{Mpc}$ are considered to be in the “1-halo regime” (galaxies within the same halo) and galaxies outside this range are in the “2-halo regime” (galaxies residing in separate halos).

2.2. Dataset Generation

To train `IAEmu`, we generate galaxy catalogs using `halotools-IA`, incorporating seven HOD and IA parameters derived from an existing dark matter halo catalog that is consistent with a realistic cosmology. We use dark matter catalogs from the Bolshoi-Planck (Bol-Planck) simulations, which are available directly through `halotools-IA` for this purpose (Klypin et al. 2011). We populate halos with galaxies following occupation equations from Zheng et al. (2007). To choose physically plausible values for the five occupation parameters used by these two models, we select the best-fit HOD parameter values for the Sloan Digital Sky Survey sample from Table 1 of Zheng et al. (2007). Further details of how we employ these occupation methods as well as a discussion of the phase space and alignment models are given in Appendix A.

The five occupation parameters are: $\log M_{\min}$, $\log M_0$, $\log M_1$, α , and $\sigma_{\log M}$. The parameters $\log M_{\min}$, $\log M_0$, and $\log M_1$ control the relationship between dark matter halo masses and the likelihood of hosting central and satellite galaxies in the HOD model. Specifically, $\log M_{\min}$ defines the minimum halo mass required to host a central galaxy, $\log M_0$ sets the mass scale associated with the suppression of the satellite galaxy occupation, and $\log M_1$ determines the amplitude of the satellite occupation profile. The number of galaxies in a given catalog ranges from 10^5 to 10^6 , with the average number decreasing with larger $\log M_{\min}$. The parameter α describes the asymptotic slope of satellite occupation at

high halo masses, while $\sigma_{\log M}$ characterizes the width of the transition between halos that do and do not host central galaxies. Figure 1 shows the regions from which four of the five occupation model parameters are drawn.

The two alignment parameters, μ_{cen} and μ_{sat} , govern the shape of the Dimroth-Watson distribution from which galaxy misalignments are sampled, as introduced in Van Alfen et al. (2024). More specifically, an alignment parameter value of 0 corresponds to a uniform distribution in $\cos(\theta)$, where θ is the galaxy misalignment angle, indicating randomly oriented galaxies. Values approaching 1 indicate perfectly aligned galaxies, while values approaching -1 correspond to perpendicular alignments.

To generate training data, we generate evenly spaced values of $\log M_{\text{min}}$ within the range [11, 15]. For each of these points, we draw a value for each of the other four occupation parameters uniformly from a region ± 4 -RMSE around the linear fit to $\log M_{\text{min}}$, where RMSE refers to the root mean squared error between the observed values of each occupation parameter and their corresponding values predicted by the linear fit. The two alignment parameters, μ_{cen} and μ_{sat} , are each sampled uniformly on $[-1, 1]$. The sampling procedure was designed to yield physically viable configurations for training IAEmu. It was observed that certain input configurations could lead to an absence of galaxies in specific bins, resulting in NaN values in the correlation functions. This issue frequently arises at small scales, or when the values of $\log M_{\text{min}}$ are sufficiently large, making the halos that host galaxies rare. To address this, such cases were removed. Additionally, as a further screening measure, we impose a restriction on input configurations that yield ξ/ξ_{DM} values exceeding 100, as these are deemed unphysical.

With these input parameter values, we generate galaxy catalogs using `halotools-IA` and measure the three correlations described in Section 2.1. As HOD modeling is inherently stochastic, we generate 10 realizations of a galaxy catalog for each given set of input values for training. The multiple realizations can enable IAEmu to distinguish the signal from the shape noise of the data, and they later serve to quantify the performance of IAEmu for the noisier correlations. As discussed in more detail in Appendix D of Van Alfen et al. (2024), shape noise dominates over sample variance in the HOD models used for ω and η correlations. Thus, we can capture most of the statistical variance by re-aligning galaxies through these extra realizations. The final dataset has 110,526 parameter choices, with 10 realizations, for a total of 1,105,260 entries. These are split into a 70% train, 10% validation, and 20% test set with unique input parameters in each subset. The training data was generated using a combination of 2.4 GHz Intel E5-2680 CPUs and 2.1 GHz Intel Xeon Platinum 8176 CPUs. The simulations were parallelized across 150 cores, split evenly to allow simultaneous calculation of the correlation functions.

3. THE IAEMU MODEL

In this section, we summarize the IAEmu architecture and training procedure.

3.1. Model Architecture

Our objective is to construct a neural network (NN) that replicates the mapping between HOD simulations and correlation function estimators. Specifically, the NN will take a 7-dimensional input vector of galaxy HOD and IA parameters, as described in Section 2 and illustrated in Figure 2, and predict the correlation functions $\xi(r)$, $\omega(r)$, and $\eta(r)$ across 20 bins. We represent each correlation function by a vector recording the value for 20 evenly spaced values of r . Additionally, the model directly outputs predictions of the aleatoric uncertainties σ^{aleo} of the correlation amplitudes. This allows us to capture the stochastic nature of HOD modeling through a mean-variance estimation (MVE) training procedure (Nix & Weigend 1994). Separately, we use Monte Carlo dropout to track the epistemic uncertainties σ^{epi} inherent in the NN model. These can arise from limited training data or architecture misspecification. Both types of uncertainties are useful for analyzing $\omega(r)$ and $\eta(r)$ performance, which are inherently noisier statistics due to the significant effects of galaxy shape noise in correlations (Bernstein & Jarvis 2002). Mathematically, the task mapping is a function

$$f_{\phi}: \mathbb{R}^7 \rightarrow \mathbb{R}^{2 \times 20} \times \mathbb{R}^{2 \times 20} \times \mathbb{R}^{2 \times 20}$$

where f_{ϕ} maps the input X to a set of mean and aleatoric uncertainty pairs:

$$X \mapsto \left(\underbrace{[\mu_{\xi}, \sigma_{\xi}^{\text{aleo}}]}_{\in \mathbb{R}^{2 \times 20}}, \underbrace{[\mu_{\omega}, \sigma_{\omega}^{\text{aleo}}]}_{\in \mathbb{R}^{2 \times 20}}, \underbrace{[\mu_{\eta}, \sigma_{\eta}^{\text{aleo}}]}_{\in \mathbb{R}^{2 \times 20}} \right).$$

We implement f_{ϕ} as an NN called IAEmu using PyTorch (Paszke et al. 2019). The IAEmu architecture includes a fully connected embedding network and three 1D convolutional NN decoder heads, trained using a multitask learning approach as shown in Figure 2.

The embedding network contains five fully connected linear layers, each followed by batch normalization and LeakyReLU activation (Xu et al. 2015). There are also residual connections in the third and fourth layer, allowing for improved information flow and gradient stability across the network (He et al. 2015). The embedding network increases the size of the input vector $X \in \mathbb{R}^7$ layer-by-layer to a 256-dimensional latent feature, which is then mapped through a final bottleneck layer to a 128-dimensional latent vector v . To mitigate overfitting, we implement dropout (Srivastava et al. 2014). As described later, we also use dropout to isolate the epistemic uncertainty associated with the model’s parameters through the Monte Carlo dropout technique (Gal & Ghahramani 2016).

The decoders each contain seven 1D convolutional decoder layers. Each decoder first takes the output of the embedding network, a feature vector v of size 128, and maps it into an expanded feature space. This expanded feature vector is then reshaped to create a multi-channel 1D feature map, enabling the decoder to utilize 1D convolution to spatially transform the latent representation. Each layer has batch normalization, LeakyReLU activation, and dropout. Residual connections are introduced by adding the output of the second convolutional layer to the output of the third layer and by adding the output of the fifth layer to the output of the sixth layer. Each decoder gradually downsamples the latent repres-

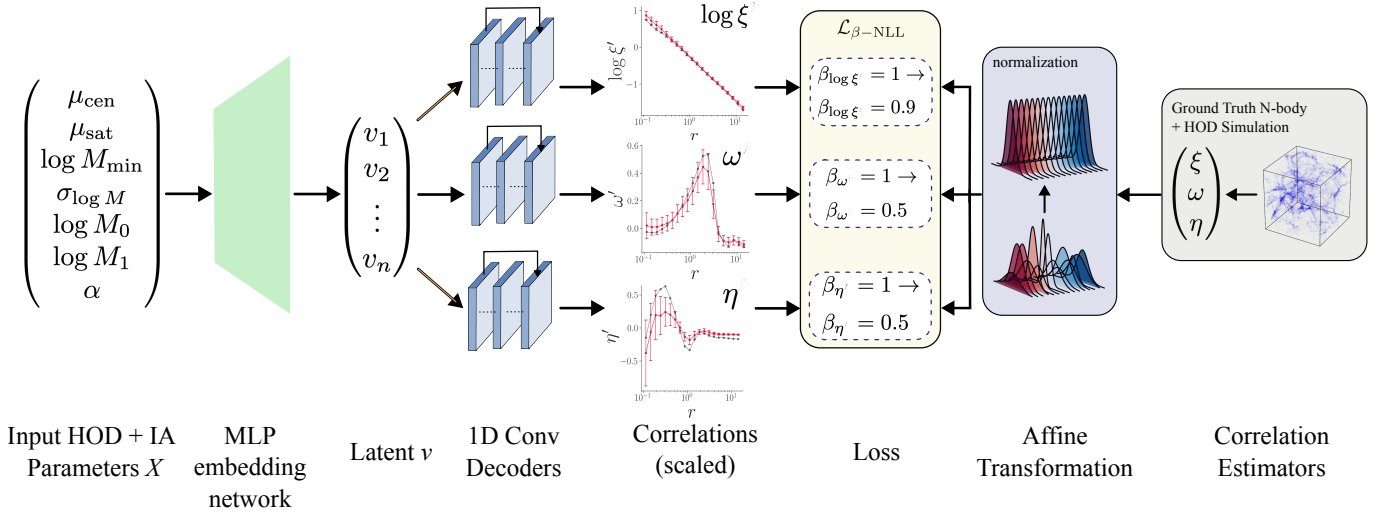


Figure 2. Model Pipeline. The HOD input model parameters are normalized before entering the 7-layer deep fully-connected embedding network. The embedding network expands the dimensionality of the input before a bottleneck latent space that transitions to the decoder stage, which features seven 1D convolutional layers which learn the individual local correlations present in the output correlation functions, $\log \xi$, ω , and η . Both the embedding network and decoder feature residual connections, visualized as dotted arrows, to aid the convergence of IAEmu during training. IAEmu is trained using the β -NLL loss (Seitzer et al. 2022) with a 100 epoch warm-up period corresponding to mean-squared-error optimization before re-introducing aleatoric uncertainties into the optimization. The outputted correlation functions are then re-scaled back to their original values. A detailed description of the model training procedure is shown in Appendix C. N-body simulation visualization in the right panel is from (Peraudin et al. 2019).

entation v and finally outputs a 2-channel 1D signal as a tensor of shape 2×20 where the 2 channels represent the correlation amplitudes and variances respectively of the correlation function. To ensure variances are strictly positive, they are passed through a `softplus` activation in the output layer.

The IAEmu design serves a dual purpose, it facilitates vector-to-sequence conversion through the convolution of encoded representations from the embedding network and, within our multitask framework, enables separate forward paths to isolate features unique to each individual correlation estimator.

3.2. Training

We now describe the training procedure for IAEmu. We normalize each feature within the 7-dimensional input vector $X \in \mathbb{R}^7$ such that the overall distribution of each component of X has a mean of 0 and unit variance. That is, each individual feature x (i.e., a single component of X) undergoes the transformation:

$$x' = \frac{x - \mu_x}{\sigma_x}, \quad (5)$$

where μ_x and σ_x are the mean and standard deviation of the respective feature across the entire training dataset. This is an *affine* transformation and is thus easily invertible.

We are interested in predicting three sequences, each of length 20, corresponding to the correlation functions $\xi(r)$, $\omega(r)$, and $\eta(r)$ for $0.1 h^{-1} \text{Mpc} < r < 16 h^{-1} \text{Mpc}$. Since these correlations exhibit different magnitudes and characteristics, each correlation function is also standardized separately for the training of IAEmu. This ensures that each correlation is scaled to have a mean of 0 and unit variance across all bins. Without this, the loss

landscape would be unevenly influenced by the differing magnitudes of the correlation functions. For example, $\xi(r)$ can exhibit strong correlations at low values of r , reaching amplitudes on the order of 10^4 or higher. In contrast, $\omega(r)$ and $\eta(r)$ exhibit amplitudes several orders of magnitude smaller than $\xi(r)$, and can also frequently take on negative values. Applying separate standardization to each correlation function ensures that all three contribute equally to the loss landscape during training. Since ξ can vary over several orders of magnitude, we take its logarithm before z-score standardization. This transformation reduces skewness and can help mitigate the dominance of high-magnitude correlations in the standardization process. We thus denote the IAEmu predicted correlations as $\log \hat{\xi}(r)$, $\hat{\omega}(r)$, and $\hat{\eta}(r)$. This standardization additionally applies to the IAEmu predicted aleatoric uncertainties: $\widehat{\sigma}_{\log \xi}^{\text{aleo}}$, $\widehat{\sigma}_{\omega}^{\text{aleo}}$, and $\widehat{\sigma}_{\eta}^{\text{aleo}}$, as well as to the epistemic uncertainties: $\widehat{\sigma}_{\log \xi}^{\text{epi}}$, $\widehat{\sigma}_{\omega}^{\text{epi}}$, and $\widehat{\sigma}_{\eta}^{\text{epi}}$. All presented results are for rescaled correlations and uncertainties, with the rescaling transformations given in Appendix B.

To predict the mean and variance of the values of the correlation function, we use the β -NLL loss from (Seitzer et al. 2022), which is defined as

$$\mathcal{L}_{\beta\text{-NLL}} = \mathbb{E}_{X,Y} \left[\hat{\sigma}^{2\beta}(X) \left(\frac{1}{2} \log \hat{\sigma}^2(X) + \frac{(Y - \hat{\mu}(X))^2}{2\hat{\sigma}^2(X)} + C \right) \right] \quad (6)$$

This is similar to Gaussian-NLL loss (Nix & Weigend 1994), defined

$$\mathcal{L}_{\text{NLL}} = \mathbb{E}_{X,Y} \left[\frac{1}{2} \log \hat{\sigma}^2(X) + \frac{(Y - \hat{\mu}(X))^2}{2\hat{\sigma}^2(X)} + C \right], \quad (7)$$

where X denotes the input data vector, $\hat{\mu}(X)$ and $\hat{\sigma}^2(X)$ the model predictions at an individual bin, and Y the ground truth label. The numerator of the second term in Equation 7 is the typical mean-squared-error loss, used when the model only outputs a point estimate approximating the mean of the distribution. One drawback of the Gaussian NLL loss is that the model can become stuck in local minima in the loss landscape during training. This results in a prediction with an incorrect mean and high variance. However, by adjusting β appropriately, this risk can be reduced. The utility of the β -NLL loss can be seen in the gradients:

$$\begin{aligned}\nabla_{\hat{\mu}} \mathcal{L}_{\beta\text{-NLL}}(\theta) &= \mathbb{E}_{X,Y} \left[\frac{\hat{\mu}(X) - Y}{\hat{\sigma}^{(2-2\beta)}(X)} \right] \\ \nabla_{\hat{\sigma}^2} \mathcal{L}_{\beta\text{-NLL}}(\theta) &= \mathbb{E}_{X,Y} \left[\frac{\hat{\sigma}^2(X) - (Y - \hat{\mu}(X))^2}{2\hat{\sigma}^{(4-2\beta)}(X)} \right].\end{aligned}$$

The β parameter allows one to interpolate between Gaussian-NLL in the limit that $\beta \rightarrow 0$, and standard MSE in the limit that $\beta \rightarrow 1$. This loss has the benefit of allowing one to encode the strength of the mean prediction to the loss, to discourage local minima with poor mean predictions and large variances. It was empirically found in Seitzer et al. (2022) that a value of $\beta = 0.5$ generally performs best. However, we explore different values of β and introduce a warm-up period of ℓ' epochs to enable individualized training for each correlation. The total loss function during training at epoch ℓ is:

$$\mathcal{L}(\ell; \theta) = \begin{cases} \mathcal{L}_{\beta\text{-NLL}}^{\xi}(\theta, 1.0) + \mathcal{L}_{\beta\text{-NLL}}^{\omega}(\theta, 1.0) & \text{if } \ell < \ell' \\ \mathcal{L}_{\beta\text{-NLL}}^{\eta}(\theta, 1.0) & \\ \mathcal{L}_{\beta\text{-NLL}}^{\xi}(\theta, 0.9) + \mathcal{L}_{\beta\text{-NLL}}^{\omega}(\theta, 0.5) & \text{if } \ell \geq \ell' \\ \mathcal{L}_{\beta\text{-NLL}}^{\eta}(\theta, 0.5) & \end{cases} \quad (8)$$

where we set $\beta_{\xi} = 0.9$ after the warm-up as this is a higher-signal correlation. Further details regarding the training hyperparameters can be found in Appendix C.

4. RESULTS

We analyze the performance of **IAEmu**, first on the held-out (in-distribution) test set, and further on a set of IA observations from the IllustrisTNG suite of hydrodynamical simulations. **IAEmu** achieves high average accuracy for both galaxy position-position and position-orientation statistics, and demonstrates robustness to shape noise in the orientation-orientation statistics without signs of overfitting. We show that **IAEmu**'s performance on η is more difficult to quantify due to the high stochasticity of the correlation function, even after averaging over multiple realizations of the data. We lastly show that when fitting alignment parameters to IA correlations from IllustrisTNG, **IAEmu** has better than 0.4σ agreement with **halotools-IA**.

4.1. Performance

Accuracy. We evaluate the model on the 20% in-distribution but held-out test set, as summarized in Figure 3. All test-set predictions are mean predictions averaged over 50 forward passes (i.e., predictions with Monte

Carlo Dropout) of **IAEmu**, so that an epistemic uncertainty on predictions can be retrieved. In reporting metrics, we exclude outlier examples in the ω and η correlations where **IAEmu** shows a strong Spearman correlation coefficient (> 0.5) with the ground truth or its predicted amplitude is within 1σ of the true uncertainty of the data for the majority of the bins, but the fractional error exceeds a factor of 100 and 450, respectively. These extreme values would thus be artifacts from the small amplitude and inherent variability of the ground truth data, rather than actual model inaccuracies. These thresholds were chosen as they remove only $\lesssim 1\%$ of test-set predictions, while stabilizing the mean fractional error on the test set. Even with this mitigation, many instances remain in the test set where the performance of **IAEmu** is visually suitable, but features large fractional error due to these numerical artifacts.

For the position-position (ξ) correlation, the mean fractional error per bin (top panel) reaches a maximum of 10%, with **IAEmu** achieving an average error of 3.2% for ξ . The ξ performance is biased high at large r , where the ξ correlation amplitudes are small ($|\xi| \ll 1$) and approach zero. This bias may arise in part from the standardization for training, which can disproportionately emphasize regions with larger amplitudes or compress the dynamic range at small values, leading to systematic bias. Additionally, as **IAEmu** naturally predicts $\log \xi$, small residuals near zero can appear large when transformed back to linear space.

For ω , the accuracy drops at the onset of the 2-halo regime, with an average model error across all bins of 4.9% and a similar maximum of $\sim 10\%$. We also find that the median fractional error across all bins is less than 10% for 66% of test-set predictions. This is approaching the accuracy for IA modeling likely required for Stage IV surveys (Paopiamsap et al. 2024). The mean fractional error for orientation-orientation (η) is significantly higher, averaging 54%. However, it is important to note that the ground truth ω and η correlations – even after averaging over 10 realizations of the dataset – are generally noisy and can often fluctuate between positive and negative values. Fractional error can be an inappropriate measure in this case, as it becomes ill-defined when the amplitude of the data is close to zero or changes sign, leading to misleadingly large error values.

With this in mind, we show in the middle panel of Figure 3 the median residual in units of the dataset's true aleatoric uncertainty $\hat{\sigma}$. From this metric, it is observed that despite the large fractional error in η , the predictions of **IAEmu** remain strictly within 1σ of the ground truth correlations across all bins. This trend also holds for ω . For ξ , the residual is computed in log space in the 2-halo regime to more consistently represent the bias with how **IAEmu** was trained, and to avoid exaggerated deviations caused by exponentiating small correlation values. Despite the large stochasticity of ω and η , this indicates that **IAEmu** has learned to capture the mean behavior and not overfit to the noise fluctuations in these correlations. This provides the added benefit of capturing the “cosmic mean” of the correlations directly with **IAEmu**, which would otherwise require running multiple realizations of the underlying HOD. This can also be frequently seen in example **IAEmu** predictions for ω and η as seen in Appendix D.

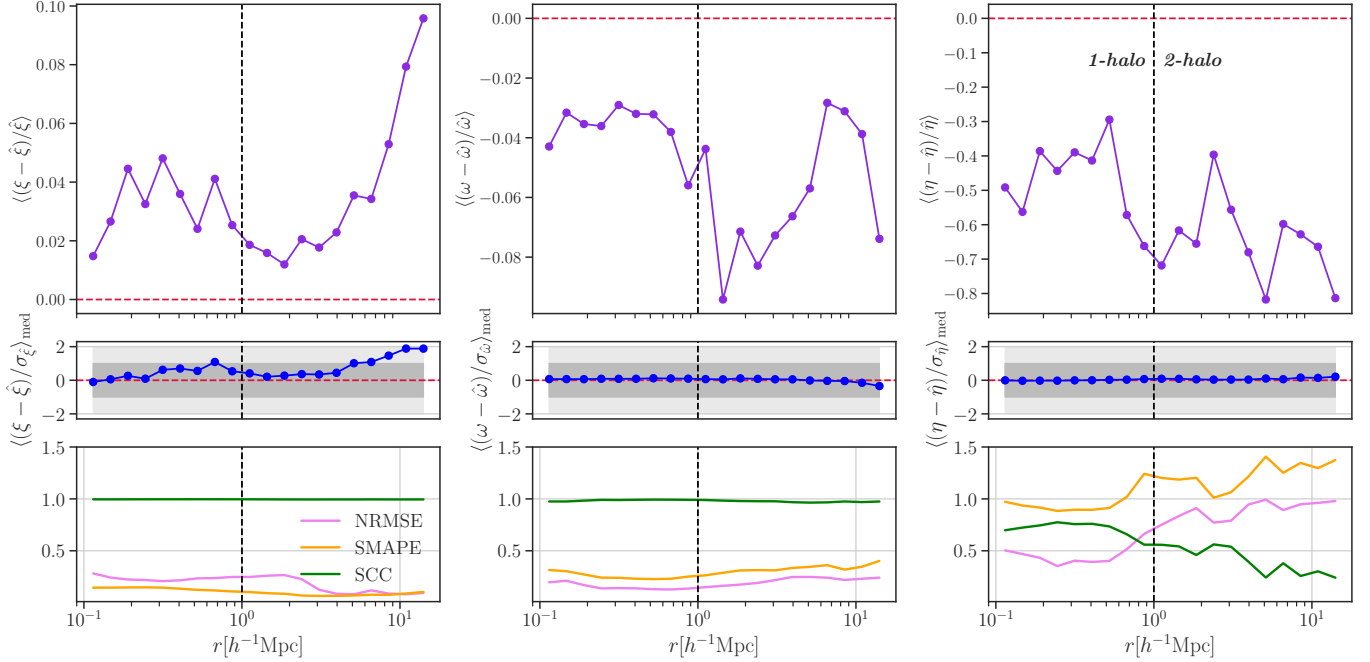


Figure 3. **Top:** Average fractional error for the position-position (ξ), position-orientation (ω), and orientation-orientation (η) correlation function predictions in the test set. **Middle:** Median residuals of the test set predictions, expressed in units of the standard deviation of the ground truth data, $\hat{\sigma}$, obtained from 10 realizations used to construct the dataset. **Bottom:** Per-bin Spearman correlation coefficient (SCC), normalized root-mean-square error (NRMSE), and symmetric mean absolute percentage error (SMAPE) for the correlation functions. A black dashed line is included in all plots to indicate the transition in r between the 1-halo and 2-halo regimes. It is seen that ξ features a 3% error, on average, and ω features a 5% error. Though exhibiting a larger fractional error, η predictions are on average strictly within 1σ of the true uncertainty. This similarly holds for ω , and ξ exhibits a bias at large r , reflecting the higher fractional error. Both ξ and ω exhibit large SCC values and low NRMSE and SMAPE values across all bins, indicating good performance. For η , the SCC value at low r ($\text{SCC} \geq 0.5$) indicates a strong correlation between **IAEmu** predictions and the ground truth. This gradually decreases at the onset of the 2-halo regime, with the NRMSE and SMAPE performance decreasing as well.

Metrics. We further evaluate the performance of **IAEmu** using three key metrics: the Spearman correlation coefficient (SCC), which measures the rank correlation between predicted and true values; the normalized root mean squared error (NRMSE); and the symmetric mean absolute percentage error (SMAPE). The SCC, which ranges between 0 and 1, is particularly useful for assessing rank-based correlations and is well-suited for analyzing sequence data. The NRMSE is defined as:

$$\text{NRMSE} = \sqrt{\frac{\frac{1}{n} \sum_{i=1}^n (y_i - \hat{y}_i)^2}{\frac{1}{n} \sum_{i=1}^n y_i^2}} \quad (9)$$

where y_i represents the ground truth value, and \hat{y}_i denotes the corresponding prediction by **IAEmu**. This metric provides an indication of prediction accuracy, but can be sensitive to outliers. To quantify relative percentage error, we use the SMAPE, which is defined

$$\text{SMAPE} = \frac{1}{n} \sum_{i=1}^n \frac{2|y_i - \hat{y}_i|}{|y_i| + |\hat{y}_i| + \epsilon} \quad (10)$$

where $\epsilon = 10^{-8}$ is introduced to prevent division by zero. The SMAPE is generally more robust to outliers compared to the NRMSE, but it tends to be more sensitive to small values. These three metrics are selected due

to their scale-invariant properties, which are essential for comparing **IAEmu**'s performance across the varying scales of ξ , ω , and η . An SCC value of 1 indicates a perfect correlation between **IAEmu** and the ground truth data, while lower values of NRMSE and SMAPE reflect better predictive performance. Together, these metrics provide a comprehensive assessment of **IAEmu**'s performance.

For ξ , we find a SCC value of 0.99 when averaged across all bins, and a value of 0.98 for ω as seen in Figure 3. This indicates a very strong correlation between the **IAEmu** predictions and the underlying data. For η , the average SCC across all bins is 0.55, with the $\text{SCC} \approx 0.75$ at low r , but is around 0.5 after entering the 2-halo regime, which still reflects a moderate correlation between the data and model. At larger r , the SCC decreases, indicating a weak correlation. It is important to note that the SCC can be strongly affected by stochasticity and the low amplitude of the data, particularly when the amplitudes approach zero, as is the case frequently for $\eta(r)$.

For ξ and ω , the NRMSE averaged across all bins is 0.19, as shown in the bottom panel of Figure 3. The corresponding SMAPE values are $\text{SMAPE}(\xi) = 0.10$ and $\text{SMAPE}(\omega) = 0.30$. The relatively low NRMSE values indicate that, on average, the predictions closely follow the ground truth across the full range of data. However, the higher SMAPE for ω compared to ξ suggests that the

relative error is more pronounced for ω , potentially due to the generally smaller correlation amplitudes in ω . This implies that while the absolute prediction error remains comparable, the percentage error is exacerbated by the lower magnitude of the true values in ω . A similar trend is observed for η , where both the NRMSE (0.69) and SMAPE (1.11) are significantly larger. These higher values indicate that **IAEmu**’s predictions for η exhibit larger absolute and relative deviations from the ground truth. This could be attributed to a decrease in performance, increased variability, or a broader dynamic range in η , which naturally poses greater challenges for accurate predictions.

Limitations. **IAEmu**’s predictions for η are less accurate compared to ξ and ω , which perform well across metrics considered. While **IAEmu** successfully captures the correct scaling of η across all bins, its accuracy for ω and η is primarily limited by the stochastic nature of these correlations, even when trained on multiple realizations and evaluated on their means. As demonstrated by examples in Appendix D, the averaged ground truth correlations still exhibit fluctuations that are indicative of noise due to the relatively small volume considered for the simulations. This hinders the evaluation of **IAEmu**’s performance as well as training; however, as also demonstrated in the middle panel of Figure 3, **IAEmu** reliably captures the underlying mean behavior despite the presence of noise. The bias in at large r for ξ can likely be attributed to the use of log and the standardization procedure for training. In a multi-task framework, standardization can potentially be avoided by using trainable loss coefficients (Kendall et al. 2018).

Efficiency. We emphasize the stark difference in speed for obtaining correlations given input HOD parameters using **IAEmu** versus **halotools-IA**. **IAEmu** performs inference on a batch of size 32,768 in 1.02 seconds on a single NVIDIA A100-80GB GPU, while the HOD, when run in parallel on 150 CPU cores for the same parameters, takes approximately 3 hours. This constitutes an approximate factor of 10^4 improvement in runtime. On a single CPU core, this would constitute an improvement of roughly 10^6 . While a direct comparison between a GPU and multiple CPU cores is inherently challenging due to differences in hardware architectures and parallelization capabilities, this comparison highlights the practical advantage of **IAEmu** in terms of computational efficiency for large-scale inference tasks with typical hardware availability. Additionally, **IAEmu**’s compatibility with differentiable sampling algorithms allows for rapid posterior estimation, further showcasing its efficiency in inverse modeling applications.

4.2. Aleatoric and Epistemic Uncertainty in **IAEmu** Predictions

Due to the high stochasticity of correlations like ω and η , **IAEmu** was designed to produce *distributions* on its outputs, tracking multiple types of uncertainty, thereby enabling confidence assessment in its predictions.

Aleatoric uncertainty represents the intrinsic variability in the data, in this case representing variance in the correlations due to galaxy shape noise and sample variance, as studied in Van Alfen et al. (2024). The aleatoric uncertainties of ω and η can thus be reduced through a larger simulation box size (resulting in more

galaxies) and through multiple realizations of the same volume. Shape noise dominates over sample variance in the HOD model predictions on the scales considered here (Van Alfen et al. 2024), making multiple realizations important for retrieving accurate correlation functions. Epistemic uncertainties are uncertainties inherent to a model and can be large when an architecture is ill-suited for a task, or when a model is not trained on sufficient data (Hüllermeier & Waegeman 2021). Aleatoric uncertainties are directly output from **IAEmu** through its design and training procedure. Epistemic uncertainties are obtained via the Monte Carlo dropout technique (Gal & Ghahramani 2016), where dropout is used during inference across multiple forward passes. This introduces stochasticity into **IAEmu**’s predictions, and the resulting variance in the outputs represents the epistemic uncertainty (see Hüllermeier & Waegeman (2021) for a review on distinguishing between aleatoric and epistemic uncertainty).

Figure 4, which compares the aleatoric and epistemic uncertainties from **IAEmu** with the true aleatoric uncertainty from **halotools-IA** across 10 realizations of the simulation. The figure shows that epistemic uncertainties are generally smaller than aleatoric uncertainties, as indicated by the majority of scatter points falling below the 1:1 line. This suggests that **IAEmu**’s architecture is sufficiently expressive for this task, and that it was not data-limited during training despite the stochasticity of these correlations. However, a median bias of 0.34 dex for ω and 0.18 dex for η for aleatoric uncertainties when compared to the true aleatoric uncertainties is observed, suggesting that **IAEmu** is not perfectly calibrated for aleatoric uncertainties. This residual is particularly pronounced near the 1:1 line, wherein **IAEmu**’s epistemic uncertainty predictions are comparable to the aleatoric uncertainty predictions. That is, **IAEmu** is prone to overestimate aleatoric uncertainties when it is more uncertain of the correlation amplitudes. Nevertheless, the shape noise estimates from **IAEmu** can provide valuable covariance information for Monte Carlo inference (Berman et al. 2025), significantly improving posterior constraints compared to inference without covariance information.

We also study the relationship between aleatoric and epistemic uncertainties in terms of the residuals in the correlation amplitudes, as shown in Figure 5. For ω , we observe a trend where the largest errors in the correlation amplitudes occur in the regime where the epistemic uncertainties are 1 dex smaller than the predicted aleatoric uncertainties. This trend is more pronounced for η , where the highest errors occur when the aleatoric uncertainties are 2 dex larger than **IAEmu**’s epistemic uncertainties, as seen in Figure 4. This may indicate an overconfidence for **IAEmu** predictions of η in this regime; however, it is also clear in comparing Figure 4 and Figure 5 that this regime is where the η correlations are noisiest. It is thus expected that the residual on **IAEmu** predictions would be exaggerated due to **IAEmu** not overfitting to the shape noise. Nonetheless, this regime is also where **IAEmu** aleatoric uncertainty predictions are the most accurate.

These insights lead us to the following conclusions about the performance of **IAEmu** for ω and η , and provide a useful diagnostic for gauging its accuracy in the absence of **halotools-IA** ground truth data:

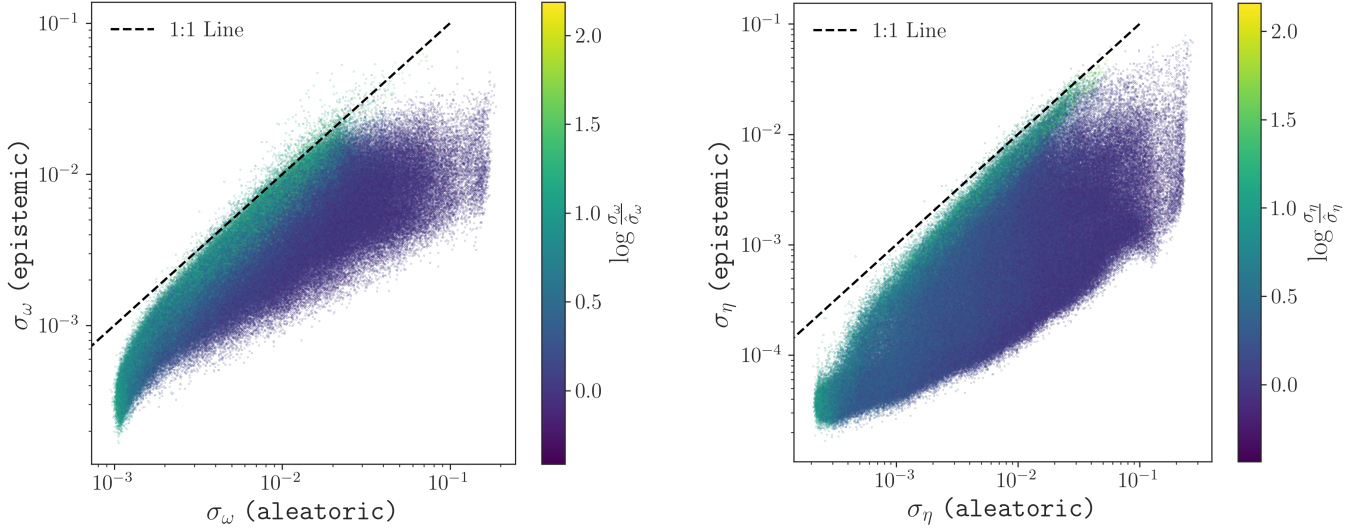


Figure 4. Aleatoric vs. epistemic uncertainty comparison for ω and η with uncertainty bias. For test-set predictions, we analyze the total spread of aleatoric uncertainties of the data predicted by **IAEmu** and epistemic uncertainties due to the stochasticity of **IAEmu**. The coloring corresponds to the log-residual between **IAEmu** predicted aleatoric uncertainties and (true) aleatoric uncertainties from **halotools-IA** produced from the 10 realizations used in producing the dataset. It is seen that the epistemic uncertainty is generally smaller than the aleatoric uncertainty, due to the majority of the scatter falling below the 1:1 line in aleatoric-epistemic uncertainty space. A general bias of 0.42 dex for ω and 0.24 dex for η is observed between the true and predicted aleatoric uncertainties, with **IAEmu** uncertainty estimates being biased high. This is exacerbated near the 1:1 line, in which the epistemic uncertainty of **IAEmu** is comparable to the predicted aleatoric uncertainty.

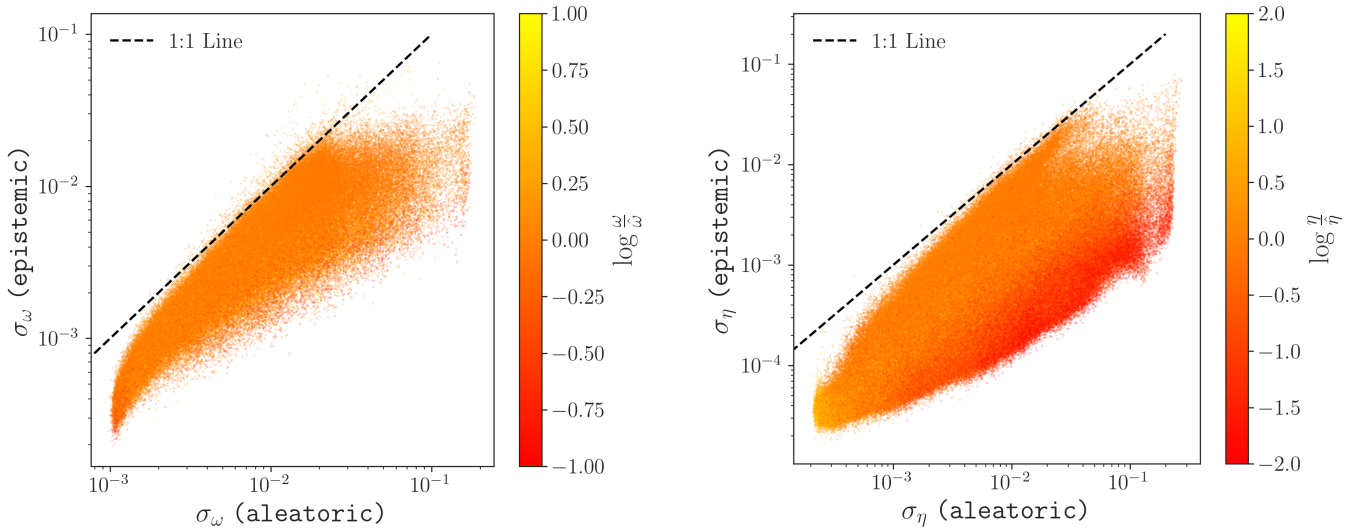


Figure 5. Aleatoric vs. epistemic uncertainty comparison for ω and η with correlation amplitude bias. For test-set predictions, we analyze the total spread of aleatoric uncertainties of the data predicted by **IAEmu** and epistemic uncertainties due to the stochasticity of **IAEmu**. The coloring corresponds to the log-residual between **IAEmu** predicted correlation amplitudes and (mean) ground truth amplitudes from **halotools-IA** produced from the 10 realizations used in producing the dataset. It is seen that there is no clear correlations between residuals in the amplitudes and **IAEmu** aleatoric and epistemic uncertainties in the case of ω . For η , it is seen that the sharpest log-residual occurs for predictions in the region where the **IAEmu** aleatoric uncertainty is ≈ 2 dex larger than the associated epistemic uncertainties. This can be an instance of **IAEmu** overfitting, wherein the intrinsic uncertainty of the model on the correlation amplitude is negligible compared to the correlations own uncertainty.

- **IAEmu** is not limited by data, as evidenced by the scale of its epistemic uncertainties compared to aleatoric uncertainties for both ω and η .
- **IAEmu** residuals on correlation amplitudes are largest when both the true and predicted aleatoric uncertainties of IA correlations are large, which is typically an artifact of **IAEmu** learning the mean behavior of these noisier statistics.
- **IAEmu** tends to overestimate aleatoric uncertainties for both ω and η in regimes where they are comparable to the epistemic uncertainties. This is when the model is most uncertain. **IAEmu** correlation amplitudes are still accurate in this regime, as shown in Figure 5.
- **IAEmu** aleatoric uncertainty predictions are most accurate for regions of parameter space that yield the noisiest correlations. This can be attributed to stronger gradient information with larger variance magnitudes, as seen in the Equation 7.

In practice, one may consider both the aleatoric and epistemic uncertainties predicted by **IAEmu** to assess the quality of its predictions in the absence of an underlying **halotools-IA** ground truth. Despite the observed bias, aleatoric uncertainty remains valuable for covariance estimation (e.g., accounting for shape noise) when performing parameter inference with **IAEmu** (Berman et al. 2025). Post-hoc calibration methods, such as those discussed in Grandón & Sellentin (2022), can help correct for these biases in parameter inference. Even when the primary concern is the correlation amplitudes, the relationship between **IAEmu**’s epistemic and aleatoric uncertainties provides valuable insight into the reliability of the predictions, as illustrated in Figures 4 and 5.

4.3. Parameter Estimation with IllustrisTNG

Our results in the previous section were obtained using a test set held out during training from the HOD simulation dataset. This demonstrates that the model generalizes well to novel data drawn from the same distribution as the training set. Previously, Van Alfen et al. (2024) showed that **halotools-IA** is expressive enough to model the IA signal derived from The IllustrisTNG300 suite of hydrodynamical simulations, which incorporate more complex physics, including baryonic effects. This constitutes an out-of-distribution (OOD) shift over the joint distribution of inputs and outputs from an HOD that **IAEmu** was trained on. In this section, we investigate whether **IAEmu** exhibits a similar modeling capability as **halotools-IA**, and can thus be robust to OOD shifts for inverse modeling. To this end, we select the best-fit occupation model parameters that reproduce the HOD of TNG300, as described in Van Alfen et al. (2024), and determine the posterior distributions on μ_{cen} and μ_{sat} that fit the signal. This is to ensure that halos with comparable masses are populated with a comparable number of galaxies as in TNG300, leaving galaxy alignment as the major factor affecting how similar correlations from the two samples are. This experiment therefore enables us to investigate potential biases between **IAEmu** and **halotools-IA** in the alignment parameter input space when modeling IA for an OOD sample. To perform

parameter inference, we leverage the differentiability of **IAEmu** to attain efficient posterior estimates. One of the advantages of **IAEmu**, and neural networks in general, is its ability to act as a differentiable forward model. This property is particularly useful for inverse problems, where the goal is to perform parameter inference based on given observations. By exploiting this differentiability, one can employ a range of differentiable sampling algorithms to obtain posterior distributions for the parameters. While Van Alfen et al. (2024) used MCMC for this purpose, we instead use Hamiltonian Monte Carlo (HMC) (Duane et al. 1987) to achieve posterior estimates more efficiently by leveraging the gradient information inherent in **IAEmu**. Further theoretical background for HMC can be found in Appendix C.

We employ two different methods: **IAEmu** with HMC and **halotools-IA** with MCMC. In both cases, we model ω by applying a uniform prior on the alignment parameters: $\mu_{\text{cen}}, \mu_{\text{sat}} \sim U(-1, 1)$. We fit to ω because ξ lacks any dependence on the IA parameters, as it represents the galaxy clustering. In contrast, η does incorporate IA information; however, the noise associated with this statistic presents a much greater challenge for solving the inverse problem compared to ω . Both the HMC and MCMC experiments employed the same jackknife covariance matrix, estimated from the TNG300 data itself.

We employ Hamiltonian Monte Carlo (HMC) with the No U-Turn Sampler (NUTS, Hoffman & Gelman (2011)), using 2000 warm-up steps and an initial learning rate of 0.005, collecting 4000 posterior samples for analysis. All posteriors resulted in an effective sample size greater than 1000, and all HMC experiments were executed on a single GPU and converged in roughly one minute. For comparison, the MCMC implementation in Van Alfen et al. (2024) utilized parallelization across 150 CPU cores and required up to a full day due to computational constraints. This highlights a near 2000 \times speed-up for **IAEmu-HMC** relative to **halotools-IA-MCMC** on the tested hardware. While this is somewhat lower than the acceleration achieved in forward modeling with **IAEmu** compared to **halotools-IA**, it remains a substantial improvement. The reduced gain is anticipated: HMC necessitates backpropagation through **IAEmu**, roughly doubling the computational load compared to a forward pass (Goodfellow et al. 2016), along with added overhead from NUTS numerical integration. Additionally, HMC’s sequential nature does not allow for parallelization. Nevertheless, its rapid convergence demonstrates its efficiency over traditional, parallelized MCMC approaches. We emphasize that a detailed convergence comparison was not performed, and that the parallelized MCMC yielded approximately 75,000 posterior samples, in contrast to the 4000 obtained via **IAEmu**. Hence, the reported speed-up metrics should be interpreted as indicative benchmarks rather than definitive measurements.

The corner plots in Figure 7 show the joint $(\mu_{\text{cen}}, \mu_{\text{sat}})$ posteriors for three separate stellar mass thresholds M_* for both **IAEmu** and **halotools-IA**. Sample 1 corresponds to $\log(M_*) > 10.5$, Sample 2 to $\log(M_*) > 10.0$, and Sample 3 to $\log(M_*) > 9.5$. The HOD parameter fits corresponding to these mass cutoffs can be found in (Van Alfen et al. 2024). We confirm two trends also observed in Van Alfen et al. (2024): central alignment strength is larger than satellite alignment strength, and the align-

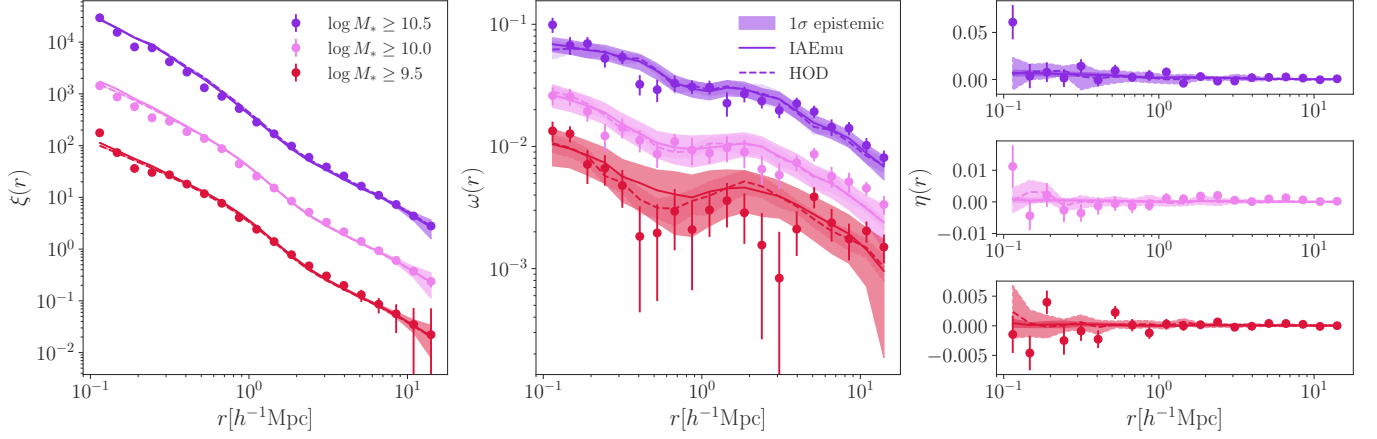


Figure 6. The two-point correlation functions (2PCFs) for IA, fitted to observations from the TNG300 simulation, using both `halotools-IA` and `IAEmu`. These 2PCFs correspond to the posterior mean values of μ_{cen} and μ_{sat} , as shown in Figure 7. Error bars for TNG300 are obtained via jackknife resampling, while the 1σ epistemic uncertainty for `IAEmu` is estimated from 50 forward passes using the Monte Carlo dropout technique. The 1σ uncertainty band for `halotools-IA` reflects variations from random realizations of the model. **Left:** Position-position correlation function ξ with the upper and lower curves offset by 1 dex for visual clarity, showing that `IAEmu` can model galaxy bias. **Middle:** Position-orientation correlation function ω . **Right:** Orientation-orientation correlation function η .

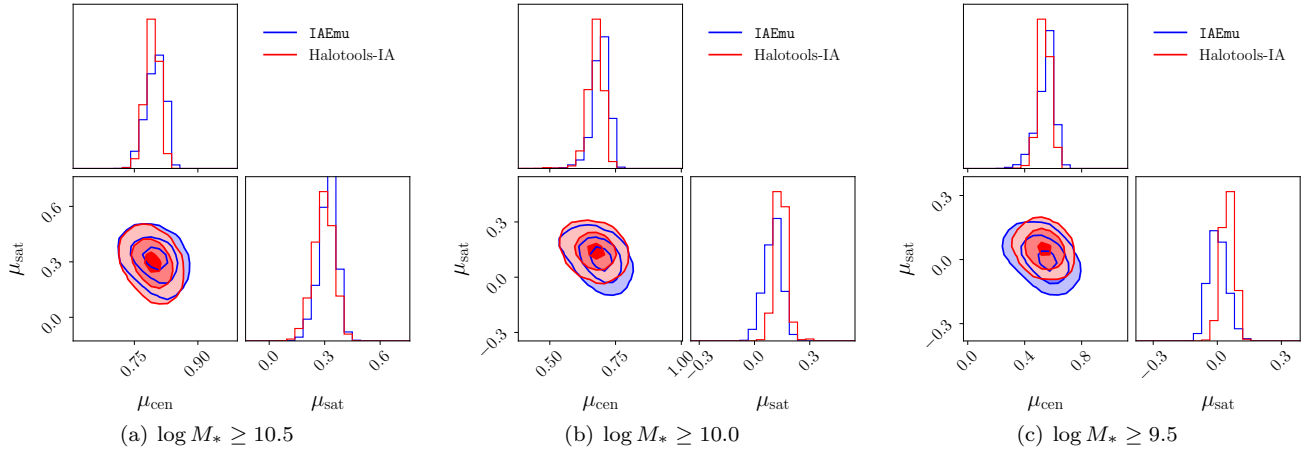


Figure 7. Optimal parameter values for central alignment strength (μ_{cen}) and satellite alignment strength (μ_{sat}) fit to observations from TNG300 with three distinct mass cutoffs for halos included in the underlying HOD model. Posterior contours for `halotools-IA` and `IAEmu` are shown with 4000 posterior samples each. Posteriors for `halotools-IA` were obtained via MCMC using 75 walkers running in parallel for 23 hours on CPU, resulting in up to 1300 steps per walker, or as few as about 450 steps per walker for slower runs. Posteriors for `IAEmu` were retrieved using NUTS, a variant of the HMC algorithm, with 2000 warm up steps around a minute on a single GPU. `IAEmu` posteriors exhibit a better than 0.4σ overlap with posteriors from `halotools-IA`, indicating that `IAEmu` can generalize to OOD shifts for inverse modeling. Exact posterior summaries for comparison can be found in Table 1. **Left:** Sample 1 `IAEmu` posteriors with optimal values $\mu_{\text{cen}} = 0.81$ and $\mu_{\text{sat}} = 0.35$. **Middle:** Sample 2 `IAEmu` posteriors with optimal values $\mu_{\text{cen}} = 0.70$ and $\mu_{\text{sat}} = 0.14$. **Right:** Sample 3 `IAEmu` posteriors with optimal values $\mu_{\text{cen}} = 0.52$ and $\mu_{\text{sat}} = 0.01$.

ment strength monotonically increases with the stellar mass threshold. We find a greater than 0.4σ agreement between MCMC with `halotools-IA` and HMC with `IAEmu` for all samples. The strongest discrepancy is in the posterior variance for Sample 3, which is the noisiest set of Illustris data and also has the largest `IAEmu` epistemic uncertainty, as seen in Figure 6. This reflects the discussion in Section 4.2, wherein it was seen that the epistemic uncertainty of `IAEmu` is correlated with the true and predicted aleatoric uncertainty. Exact values

for `halotools-IA` and `IAEmu` posterior summary statistics are shown in Table 1.

The correlation function predictions from `IAEmu` with posterior means for μ_{cen} and μ_{sat} are shown in Figure 6, in which we see that there is generally good agreement with `IAEmu` predictions compared to those from `halotools-IA` for all correlations. The correlation function, ξ , is also shown to illustrate the agreement between `halotools-IA` and `IAEmu` for galaxy clustering statistics; however, it does not depend on μ_{cen} or μ_{sat} .

Table 1. Posterior values for IAEmu and `halotools-IA` fit on TNG300.

Sample	Mass Cutoff	Posterior	μ_{cen}	μ_{sat}
1	$\log M_* > 10.5$	IAEmu	$0.80^{+0.02}_{-0.03}$	$0.32^{+0.04}_{-0.05}$
		<code>halotools-IA</code>	$0.79^{+0.02}_{-0.02}$	$0.30^{+0.05}_{-0.06}$
2	$\log M_* > 10.0$	IAEmu	$0.69^{+0.03}_{-0.03}$	$0.11^{+0.04}_{-0.05}$
		<code>halotools-IA</code>	$0.68^{+0.03}_{-0.03}$	$0.14^{+0.03}_{-0.03}$
3	$\log M_* > 9.5$	IAEmu	$0.56^{+0.04}_{-0.07}$	$0.00^{+0.05}_{-0.04}$
		<code>halotools-IA</code>	$0.54^{+0.04}_{-0.04}$	$0.05^{+0.03}_{-0.03}$

5. SUMMARY & DISCUSSION

In this work, we have developed a neural network-based surrogate model, **IAEmu**, designed to predict galaxy intrinsic alignment correlations derived from halo occupation distribution modeling. **IAEmu** eliminates the need to generate full galaxy catalogs and compute correlation functions using traditional HOD pipelines, which are computationally expensive. On a single GPU, **IAEmu** achieves a $\times 10^4$ speed-up in wall-clock time compared to `halotools-IA` run on a moderately parallelized CPU setup representative of typical resources (e.g., ~ 150 cores). When comparing single GPU to single CPU performance, this corresponds to an approximate $10^6 \times$ speed-up. This substantial acceleration enables efficient forward modeling and significantly expedites inverse modeling tasks. The differentiable nature of **IAEmu** facilitates the use of gradient-based inference methods such as Hamiltonian Monte Carlo (HMC), which are otherwise infeasible with `halotools-IA`. Although the speed-up in individual evaluations is dramatic, the end-to-end improvement in sampling-based inference compared to parallelized MCMC is somewhat lower, due to the additional computational overhead from gradient evaluations and the inherently sequential nature of HMC arising from numerical trajectory integration. Nevertheless, HMC achieves significantly faster convergence than parallelized MCMC, making it a far more efficient option overall for inverse modeling despite the reduced relative speed-up.

IAEmu was also designed to account for both aleatoric and epistemic uncertainties, corresponding to the uncertainty inherent in the data and the model, respectively. This enables confidence assessments for **IAEmu** predictions in the absence of ground truth data, as well as provides covariance information for inverse modeling with **IAEmu**. To isolate aleatoric uncertainty, we trained **IAEmu** using a mean-variance estimation framework under the assumption of Gaussian-distributed outputs, optimized with the β -negative-log-likelihood loss function. For epistemic uncertainty, we employed the Monte Carlo dropout technique, which randomly nullifies certain nodes within **IAEmu** during inference, introducing stochasticity into the model predictions. We find that analyzing these distinct sources of uncertainty provides valuable insight into the strengths and weaknesses of **IAEmu**, offering a practical method for diagnosing the quality of emulator predictions and motivating future improvements.

Challenges. The **IAEmu** architecture and training algorithm were tailored to address the challenging goal of simultaneously modeling galaxy bias and IA correlations

from a given set of HOD and alignment parameters. Architecturally, **IAEmu** employs a fully connected embedding network with a 1D convolutional neural network decoder, which features multiple branches. The shared encoded representation captures the common features of HOD simulations relevant to all correlations, while the separate decoder branches are intended to learn the estimators for each correlation function. The 1D convolutional layers are crucial for identifying local structures within the encoded representations and for facilitating the transition from input feature vectors to correlation function sequences. Additionally, **IAEmu** incorporates residual connections and dropout layers to improve training convergence and mitigate overfitting.

Simultaneously training on three distinct correlations, each with varying scales and signal-to-noise, presented additional engineering challenges from a training perspective. In particular, the low signal-to-noise of the η correlation made accurate modeling of its uncertainties especially difficult. To address this, we implemented the β -NLL loss within a multitask learning framework. This approach ensured that correlations with larger amplitudes did not disproportionately dominate the loss landscape, while facilitating effectively individualized training for each decoder branch, allowing us to prioritize more accurate aleatoric uncertainty estimates for the noisier ω and η correlations while focusing on correlation amplitude predictions for the higher-signal ξ correlation.

Results. **IAEmu** achieves an average error of approximately 3% in emulating position-position and 5% in position-orientation galaxy IA correlations. Although the orientation-orientation correlation η is inherently noisier and thus more difficult to quantify performance for, **IAEmu**'s predictions for η on average remained within 1σ of the true aleatoric uncertainty of the data when evaluated on the test set. This indicates that **IAEmu** still successfully captures the average behavior of this correlation without overfitting to the shape noise, which would otherwise require multiple realizations of `halotools-IA`. **IAEmu** also generally exhibits strong SCC values with the data across all three correlations, indicating that despite the large fractional errors, NRMSE, and SMAPE in the case of η , **IAEmu** captures the overall shape of the correlations well.

Finally, we found that **IAEmu** has comparable performance to `halotools-IA` when used to fit the alignment parameters μ_{cen} and μ_{sat} to IA correlation measurements from the TNG300 hydrodynamic simulation, in a manner similar to the robustness test originally performed in (Van Alfen et al. 2024). This demonstrates **IAEmu**'s robustness to OOD shifts for inverse problems. Specifically, we observe a better than 0.4σ agreement in the μ_{cen} and μ_{sat} posteriors across three separate mass regimes between **IAEmu**, fit using HMC, and `halotools-IA`, fit with Markov Chain Monte Carlo (MCMC). A significant advantage was the improvement in computational efficiency; while `halotools-IA` with MCMC required approximately one day on a cluster CPU, **IAEmu** completed the inverse problem in less than a minute on a single GPU. This constitutes a nearly 2000x speed up over MCMC with `halotools-IA`, demonstrating that the efficiency benefits of neural network surrogate models extend beyond forward modeling.

Future Work. In future work, we will improve upon the IAEmu pipeline by exploring different architectural and data choices. IAEmu, as presented here, operates in a traditional supervised learning regime, where the model learns a direct, deterministic mapping between the HOD parameters and correlations. Although we introduce stochasticity for uncertainty quantification via MC dropout and MVE, a more natural probabilistic approach could be achieved through conditional diffusion generative modeling, where the model learns a probabilistic mapping via a denoising process on the data, or through flow-based architectures as in Pandey et al. (2024). These models can also be made symmetry-aware, enhancing their effectiveness in physical settings like this (see Jagvaral et al. 2023a, for an example of SO(3)-equivariant diffusion applied to IA). Diffusion models typically leverage architectures like U-Nets (Ronneberger et al. 2015), which are well-suited for denoising tasks (Schanz et al. 2023) and follow an encoder-decoder architecture similar to what was used here. The denoising training paradigm when applied to cosmology has thus far exhibited promising results in enhancing the resolution of existing simulations (Schanz et al. 2023) as well as functioning as surrogate models (Mudur et al. 2024). Other avenues for multi-task learning, such as treating the loss coefficients as trainable parameters as in (Kendall et al. 2018), can allow more effective optimization without normalization and can potentially alleviate the biased performance in ξ observed here.

Furthermore, these future avenues would open opportunities in studying the variation in cosmological parameters, a dimension not explored in this work. Here, we have only used a single underlying dark matter catalog from an N-body simulation, which implicitly reflects specific cosmological parameters. It would be exciting to explore IA modeling for varying dark matter catalogs and thus different cosmologies. In a pure HOD setting, these extensions can be expensive.

Simulation-based modeling has led to tremendous progress in understanding galaxy intrinsic alignments, particularly when compared to earlier analytic and semi-analytic methods. However, this progress has traditionally come with incurred computational expense. In this work, we have shown a compelling case in which accuracy and efficiency can be achieved with NN-based emulators for galaxy intrinsic alignments from HOD simulations. This is a significant step towards accelerating model validation strategies in preparation for data from the Rubin Observatory, Roman Space Telescope, and other Stage IV surveys.

DATA AVAILABILITY STATEMENT

The data underlying this article is publicly accessible and was derived from sources in the public domain, such as the BolshoiPlanck Catalog and halotools.

ACKNOWLEDGEMENTS

We thank Andrew Hearin and Katrin Heitmann for helpful conversations. S.P. thanks Becky Nevin and Aleksandra Ciprajanovic for useful conversations regarding uncertainty quantification. S.P. acknowledges support from the National Science Foundation under Cooperative Agreement PHY-2019786 (The NSF AI Institute for Artificial Intelligence and Fundamental Inter-

actions, <https://iaifi.org>). Y.Y. acknowledges support from the Khoury Apprenticeship program. J.B. and N.V.A. are supported in this work by NSF award AST-2206563, the US DOE under grant DE-SC0024787, and the Roman Research and Support Participation program under NASA grant 80NSSC24K0088. R.W. is supported by NSF award DMS-2134178. Data generation was conducted on the Discovery cluster, supported by Northeastern University’s Research Computing team. The machine learning computations were run on the FASRC cluster supported by the FAS Division of Science Research Computing Group at Harvard University.

REFERENCES

- Akeson R., et al., 2019, The Wide Field Infrared Survey Telescope: 100 Hubbles for the 2020s ([arXiv:1902.05569](https://arxiv.org/abs/1902.05569)), <https://arxiv.org/abs/1902.05569>
- Aricò G., Angulo R. E., Zennaro M., 2021a, [arXiv e-prints](https://arxiv.org/abs/2104.14568), p. [arXiv:2104.14568](https://arxiv.org/abs/2104.14568)
- Aricò G., Angulo R. E., Contreras S., Ondaro-Mallea L., Pellejero-Ibañez M., Zennaro M., 2021b, *MNRAS*, **506**, 4070
- Asgari M., Mead A. J., Heymans C., 2023, *The Open Journal of Astrophysics*, **6**, 39
- Bakx T., Kurita T., Elisa Chisari N., Vlah Z., Schmidt F., 2023, *J. Cosmology Astropart. Phys.*, **2023**, 005
- Berman E., et al., 2025, On Soft Clustering For Correlation Estimators: Model Uncertainty, Differentiability, and Surrogates ([arXiv:2504.06174](https://arxiv.org/abs/2504.06174)), <https://arxiv.org/abs/2504.06174>
- Bernstein G. M., Jarvis M., 2002, *The Astronomical Journal*, **123**, 583
- Blazek J., Vlah Z., Seljak U., 2015, *Journal of Cosmology and Astroparticle Physics*, **2015**, 015
- Blazek J. A., MacCrann N., Troxel M. A., Fang X., 2019, *Phys. Rev. D*, **100**, 103506
- Bridle S., King L., 2007, *New Journal of Physics*, **9**, 444
- Campos A., Samuroff S., Mandelbaum R., 2023, *MNRAS*, **525**, 1885
- Chen S.-F., Kokron N., 2023, [arXiv e-prints](https://arxiv.org/abs/2309.16761), p. [arXiv:2309.16761](https://arxiv.org/abs/2309.16761)
- Cooray A., Sheth R., 2002, *Phys. Rep.*, **372**, 1
- Delgado A. M., et al., 2023, *MNRAS*, **523**, 5899
- Duane S., Kennedy A., Pendleton B. J., Roweth D., 1987, *Physics Letters B*, **195**, 216
- Dvorkin C., et al., 2022, *Machine Learning and Cosmology* ([arXiv:2203.08056](https://arxiv.org/abs/2203.08056))
- Fortuna M. C., Hoekstra H., Joachimi B., Johnston H., Chisari N. E., Georgiou C., Mahony C., 2021, *MNRAS*, **501**, 2983
- Gal Y., Ghahramani Z., 2016, Dropout as a Bayesian Approximation: Representing Model Uncertainty in Deep Learning ([arXiv:1506.02142](https://arxiv.org/abs/1506.02142))
- Goodfellow I., Bengio Y., Courville A., 2016, *Deep Learning*. MIT Press
- Grandón D., Sellentin E., 2022, *The Open Journal of Astrophysics*, **5**
- He K., Zhang X., Ren S., Sun J., 2015, Deep Residual Learning for Image Recognition ([arXiv:1512.03385](https://arxiv.org/abs/1512.03385)), <https://arxiv.org/abs/1512.03385>
- Hirata C. M., Seljak U., 2004, *Phys. Rev. D*, **70**, 063526
- Hoffman M. D., Gelman A., 2011, The No-U-Turn Sampler: Adaptively Setting Path Lengths in Hamiltonian Monte Carlo ([arXiv:1111.4246](https://arxiv.org/abs/1111.4246)), <https://arxiv.org/abs/1111.4246>
- Hoffmann K., et al., 2022, *Phys. Rev. D*, **106**, 123510
- Hüllermeier E., Waegeman W., 2021, *Machine Learning*, **110**, 457–506
- Ivezić Z., et al., 2019, *ApJ*, **873**, 111
- Jagvaral Y., Lanusse F., Singh S., Mandelbaum R., Ravanbakhsh S., Campbell D., 2022, *Monthly Notices of the Royal Astronomical Society*, **516**, 2406–2419
- Jagvaral Y., Lanusse F., Mandelbaum R., 2023a, DIFFUSION GENERATIVE MODELS ON SO(3), <https://openreview.net/forum?id=jHA-yCyBGb>
- Jagvaral Y., Lanusse F., Mandelbaum R., 2023b, [arXiv e-prints](https://arxiv.org/abs/2312.11707), p. [arXiv:2312.11707](https://arxiv.org/abs/2312.11707)

- Jagvaral Y., Lanusse F., Mandelbaum R., 2024, [arXiv e-prints](#), p. [arXiv:2409.18761](#)
- Joachimi B., Semboloni E., Hilbert S., Bett P. E., Hartlap J., Hoekstra H., Schneider P., 2013, *Monthly Notices of the Royal Astronomical Society*, 436, 819
- Kendall A., Gal Y., Cipolla R., 2018, Multi-Task Learning Using Uncertainty to Weigh Losses for Scene Geometry and Semantics ([arXiv:1705.07115](#)), [https://arxiv.org/abs/1705.07115](#)
- Klypin A. A., Trujillo-Gomez S., Primack J., 2011, *ApJ*, 740, 102
- Krause E., Eifler T., Blazek J., 2016, *MNRAS*, 456, 207
- Kwan J., et al., 2023, *The Astrophysical Journal*, 952, 80
- Landy S. D., Szalay A. S., 1993, *ApJ*, 412, 64
- Lawrence E., Heitmann K., White M., Higdon D., Wagner C., Habib S., Williams B., 2010, *ApJ*, 713, 1322
- Loshchilov I., Hutter F., 2019, Decoupled Weight Decay Regularization ([arXiv:1711.05101](#))
- Maion F., Angulo R. E., Bakx T., Chisari N. E., Kurita T., Pellejero-Ibáñez M., 2023, [arXiv e-prints](#), p. [arXiv:2307.13754](#)
- Maksimova N. A., Garrison L. H., Eisenstein D. J., Hadzhiyska B., Bose S., Satterthwaite T. P., 2021, *Monthly Notices of the Royal Astronomical Society*, 508, 4017–4037
- Marinacci F., et al., 2018, *Monthly Notices of the Royal Astronomical Society*
- Mudur N., Cuesta-Lazaro C., Finkbeiner D. P., 2024, Diffusion-HMC: Parameter Inference with Diffusion Model driven Hamiltonian Monte Carlo ([arXiv:2405.05255](#)), [https://arxiv.org/abs/2405.05255](#)
- Naiman J. P., et al., 2018, *Monthly Notices of the Royal Astronomical Society*, 477, 1206–1224
- Nelson D., et al., 2015, *Astronomy and Computing*, 13, 12–37
- Nelson D., et al., 2017, *Monthly Notices of the Royal Astronomical Society*, 475, 624–647
- Nelson D., et al., 2021, The IllustrisTNG Simulations: Public Data Release ([arXiv:1812.05609](#))
- Nix D., Weigend A., 1994, in Proceedings of 1994 IEEE International Conference on Neural Networks (ICNN'94). pp 55–60 vol.1, [doi:10.1109/ICNN.1994.374138](#)
- Pandey S., et al., 2024, CHARM: Creating Halos with Auto-Regressive Multi-stage networks ([arXiv:2409.09124](#)), [https://arxiv.org/abs/2409.09124](#)
- Paopiamsap A., Porqueres N., Alonso D., Harnois-Deraps J., Leonard C. D., 2024, *The Open Journal of Astrophysics*, 7
- Paszke A., et al., 2019, PyTorch: An Imperative Style, High-Performance Deep Learning Library ([arXiv:1912.01703](#)), [https://arxiv.org/abs/1912.01703](#)
- Perraudin N., Srivastava A., Lucchi A., Kacprzak T., Hofmann T., Réfrégier A., 2019, *Computational Astrophysics and Cosmology*, 6
- Pillepich A., et al., 2017, *Monthly Notices of the Royal Astronomical Society*, 475, 648–675
- Pillepich A., et al., 2018, *MNRAS*, 473, 4077
- Ronneberger O., Fischer P., Brox T., 2015, U-Net: Convolutional Networks for Biomedical Image Segmentation ([arXiv:1505.04597](#)), [https://arxiv.org/abs/1505.04597](#)
- Samuroff S., Mandelbaum R., Blazek J., 2021, *MNRAS*, 508, 637
- Samuroff S., Campos A., Porredon A., Blazek J., 2024, *The Open Journal of Astrophysics*, 7, 40
- Scaramella R., et al., 2022, *Astronomy & Astrophysics*, 662, A112
- Schanz A., List F., Hahn O., 2023, Stochastic Super-resolution of Cosmological Simulations with Denoising Diffusion Models ([arXiv:2310.06929](#)), [https://arxiv.org/abs/2310.06929](#)
- Secco L. F., et al., 2022, *Phys. Rev. D*, 105, 023515
- Seitzer M., Tavakoli A., Antic D., Martius G., 2022, On the Pitfalls of Heteroscedastic Uncertainty Estimation with Probabilistic Neural Networks ([arXiv:2203.09168](#)), [https://arxiv.org/abs/2203.09168](#)
- Singh S., Mandelbaum R., Seljak U., Slosar A., Vazquez Gonzalez J., 2017, *Monthly Notices of the Royal Astronomical Society*, 471, 3827
- Sluiterman L., Cator E., Heskes T., 2023, Optimal Training of Mean Variance Estimation Neural Networks ([arXiv:2302.08875](#)), [https://arxiv.org/abs/2302.08875](#)
- Springel V., et al., 2017, *Monthly Notices of the Royal Astronomical Society*, 475, 676–698
- Srivastava N., Hinton G., Krizhevsky A., Sutskever I., Salakhutdinov R., 2014, *Journal of Machine Learning Research*, 15, 1929
- Tenneti A., Mandelbaum R., Di Matteo T., 2016, *MNRAS*, 462, 2668
- Troxel M., Ishak M., 2015, *Physics Reports*, 558, 1
- Van Alfen N., Campbell D., Blazek J., Leonard C. D., Lanusse F., Hearin A., Mandelbaum R., Collaboration T. L. D. E. S., 2024, An Empirical Model For Intrinsic Alignments: Insights From Cosmological Simulations ([arXiv:2311.07374](#))
- Villaescusa-Navarro F., et al., 2020, *The Astrophysical Journal Supplement Series*, 250, 2
- Villaescusa-Navarro F., et al., 2021, *The Astrophysical Journal*, 915, 71
- Vlah Z., Chisari N. E., Schmidt F., 2020, *J. Cosmology Astropart. Phys.*, 2020, 025
- Vlah Z., Chisari N. E., Schmidt F., 2021, *J. Cosmology Astropart. Phys.*, 2021, 061
- Xu B., Wang N., Chen T., Li M., 2015, Empirical Evaluation of Rectified Activations in Convolutional Network ([arXiv:1505.00853](#))
- Zhai Z., et al., 2019, *The Astrophysical Journal*, 874, 95
- Zheng Z., Coil A. L., Zehavi I., 2007, *The Astrophysical Journal*, 667, 760

places central galaxies at the location of their parent halo and satellite galaxies at the location of any subhalos (smaller dark matter halos that reside within the larger parent halo). We use `CentralAlignment` and `RadialSatelliteAlignment` for the alignment model components. The `CentralAlignment` component aligns the central galaxy with respect to its parent halo, and `RadialSatelliteAlignment` aligns the satellite galaxies with respect to the radial vector between the central galaxy and itself. The parameters μ_{cen} and μ_{sat} , the central and satellite alignment strengths, determine the shape of the Dimroth-Watson distribution from which the misalignment angles are drawn (Van Alfen et al. 2024).

B. CORRELATION RESCALING

Constructing an HOD model with alignment requires us to choose an occupation model component to populate dark matter halos, a phase space model component to place these galaxies within their halo, and an alignment model component to assign an orientation to the galaxies. Since we distinguish between central and satellite galaxies, we choose components for each of these steps for each of the two populations. We choose the `Zheng07Cens` and `Zheng07Sats` occupation model components for central and satellite galaxies, respectively. These components are available in `halotools` and implement Equations 2, 3 and 5 from Zheng et al. (2007). As discussed earlier, the five HOD parameters chosen for these models come from Table 1 of the same paper.

For simplicity, we use `TrivialPhaseSpace` and `SubhaloPhaseSpace` as phase space model components for the central and satellite galaxies respectively, which

As `IAEmu` outputs standardized correlations, it is crucial to properly rescale the model-predicted amplitudes, aleatoric uncertainties $\widehat{\sigma}^{\text{aleo}}$, and epistemic uncertainties $\widehat{\sigma}^{\text{epi}}$ for analysis. For ξ , we denote $\hat{\xi}$ as the (standard-

ized) model prediction, $\bar{\xi}$ refers to the ξ correlations from the training dataset used for calculating statistics, and $\widehat{\sigma_{\xi}^{\text{aleo}}}$ and $\widehat{\sigma_{\xi}^{\text{epi}}}$ are the IAEmu-predicted aleatoric and epistemic uncertainties for ξ . The reverse transformation is as follows:

$$\xi = \exp \left(\log \hat{\xi} \cdot \sigma_{\log \bar{\xi}} + \mu_{\log \bar{\xi}} \right).$$

As a result of taking the log of ξ for training, the rescaled aleatoric and epistemic uncertainties are only well-defined in log space:

$$\sigma_{\log \xi}^{\text{aleo}} = \sigma_{\log \bar{\xi}} \cdot \widehat{\sigma_{\log \bar{\xi}}^{\text{aleo}}}, \quad \sigma_{\log \xi}^{\text{epi}} = \sigma_{\log \bar{\xi}} \cdot \widehat{\sigma_{\log \bar{\xi}}^{\text{epi}}}.$$

The galaxy shape correlations ω and η had no log-scaling and therefore have a simpler inversion procedure:

$$\omega = \omega' \cdot \sigma_{\bar{\omega}} + \mu_{\bar{\omega}}, \quad \sigma_{\omega}^{\text{aleo}} = \sigma_{\bar{\omega}} \cdot \widehat{\sigma_{\bar{\omega}}^{\text{aleo}}}, \quad \sigma_{\omega}^{\text{epi}} = \sigma_{\bar{\omega}} \cdot \widehat{\sigma_{\bar{\omega}}^{\text{epi}}}.$$

The last correlation function η is rescaled similarly to ω .

C. TRAINING AND HAMILTONIAN MONTE CARLO DETAILS

Training. We train the IAEmu for a maximum of 500 epochs with a 100-epoch warm-up period and early stopping. We also employ gradient clipping for numerical stability, as the training of MVE networks can suffer from instability. The use of residual connections and a shallower embedding network than the decoder is to stabilize convergence during training. We employ various techniques to further aid the convergence of the model. Following the recommendations in (Sluijterman et al. 2023), we initialize all variance output-neurons to have a bias of zero which results in a constant variance prediction across all bins at initialization, ensuring that no bins are biased towards large variances. We additionally implement a warm-up period during training with $\beta = 1.0$ for all correlations to maximize regression on the means before transitioning to a value of $\beta_{\xi} = 0.9$ and $\beta_{\omega} = \beta_{\eta} = 0.5$ for the remainder of training. The value of β_{ξ} was chosen as $\xi(r)$ correlations exhibit a very high signal-to-noise ratio, so the aleatoric uncertainties on these correlations are generally not significant or of interest.

We use the AdamW optimizer (Loshchilov & Hutter 2019) with a training batch size of 128 and a step learning rate scheduler (10% decay at 167-epoch intervals with a starting $\text{lr} = 0.01$). Additional L2-regularization via a weight decay factor of 10^{-4} is used in the optimizer. All training was done on two NVIDIA A100-80GB GPUs. During training, IAEmu is validated every 5 epochs with an early stopping patience of 100 epochs based on the validation criteria. The validation criteria for saving the model is a linear combination of MSE and Gaussian-NLL losses computed for each correlation ξ , ω , and η .

The total MSE and NLL losses are calculated as the sum of each correlation, and the averaged validation

losses are computed over the validation dataset. The final combined validation loss \mathcal{L}_{val} is defined as:

$$\mathcal{L}_{\text{val}} = \alpha \cdot \mathcal{L}_{\text{MSE}} + (1 - \alpha) \cdot \mathcal{L}_{\text{NLL}}$$

where $\alpha = 0.7$ determines the weighting between MSE and NLL, guiding model selection based on this combined criterion.

Hamiltonian Monte Carlo. HMC is a variant of the Metropolis–Hastings algorithm, where Hamiltonian dynamics are simulated using a time-reversible, volume-preserving numerical integrator to propose transitions to new points in the state space. We use HMC to sample from a posterior distribution over the inputs x , given trained NN parameters θ and observations \mathcal{D} . This is described by

$$p(x|\mathcal{D}, \theta) \propto p(\mathcal{D}|x, \theta)p(x), \quad (\text{C1})$$

Equation C1 is a form of Bayes' Theorem where $p(\mathcal{D}|x, \theta)$ is the likelihood function and $p(x)$ is the prior distribution on x . HMC achieves this by forward modeling the dynamics of a governing Hamiltonian H :

$$H = T + U = \frac{1}{2} \mathbf{p}^T M^{-1} \mathbf{p} - \ln p(x|\mathcal{D}, \theta) \quad (\text{C2})$$

where T is the kinetic energy with mass matrix M and momentum p , which controls the exploration in parameter space, and $-\ln p(x|\mathcal{D}, \theta)$ takes the role of the potential energy U . The time-evolution of x and p is accordingly governed by Hamilton's equations. HMC thus arrives at the posterior distribution over the inputs by sequentially evolving the dynamical variables according to Hamiltonian dynamics; this of course corresponds to minimizing the potential energy, which maximizes the log probability. Hamilton's equations require gradients with respect to the Hamiltonian H , specifically $-\nabla_x \ln p(x|\mathcal{D}, \theta)$. Decomposing this with chain rule,

$$\begin{aligned} \nabla_x \ln p(x|\mathcal{D}, \theta) &= \nabla_x \ln p(\mathcal{D}|x, \theta) + \nabla_x \ln p(x) \\ &\propto \nabla_x \ln p(f_{\theta}(x)|\mathcal{D}) \\ &= \nabla_{f_{\theta}(x)} \ln p(f_{\theta}(x)|\mathcal{D}) \cdot \nabla_x f_{\theta}(x), \end{aligned}$$

where in the second line we recognize that the likelihood is implicitly a function of the outputs of IAEmu, $f_{\theta}(x)$, explicitly denoting its dependence on parameters θ . We thus see how differentiability through the forward model is leveraged in this algorithm.

D. EXAMPLE IAEMU PREDICTIONS

Randomly chosen IAEmu test-set predictions with the `halotools-IA` ground truth shown in blue, and IAEmu with 1σ epistemic uncertainties given in red.

This paper was built using the Open Journal of Astrophysics L^AT_EX template. The OJA is a journal which provides fast and easy peer review for new papers in the `astro-ph` section of the arXiv, making the reviewing process simpler for authors and referees alike. Learn more at <http://astro.theoj.org>.

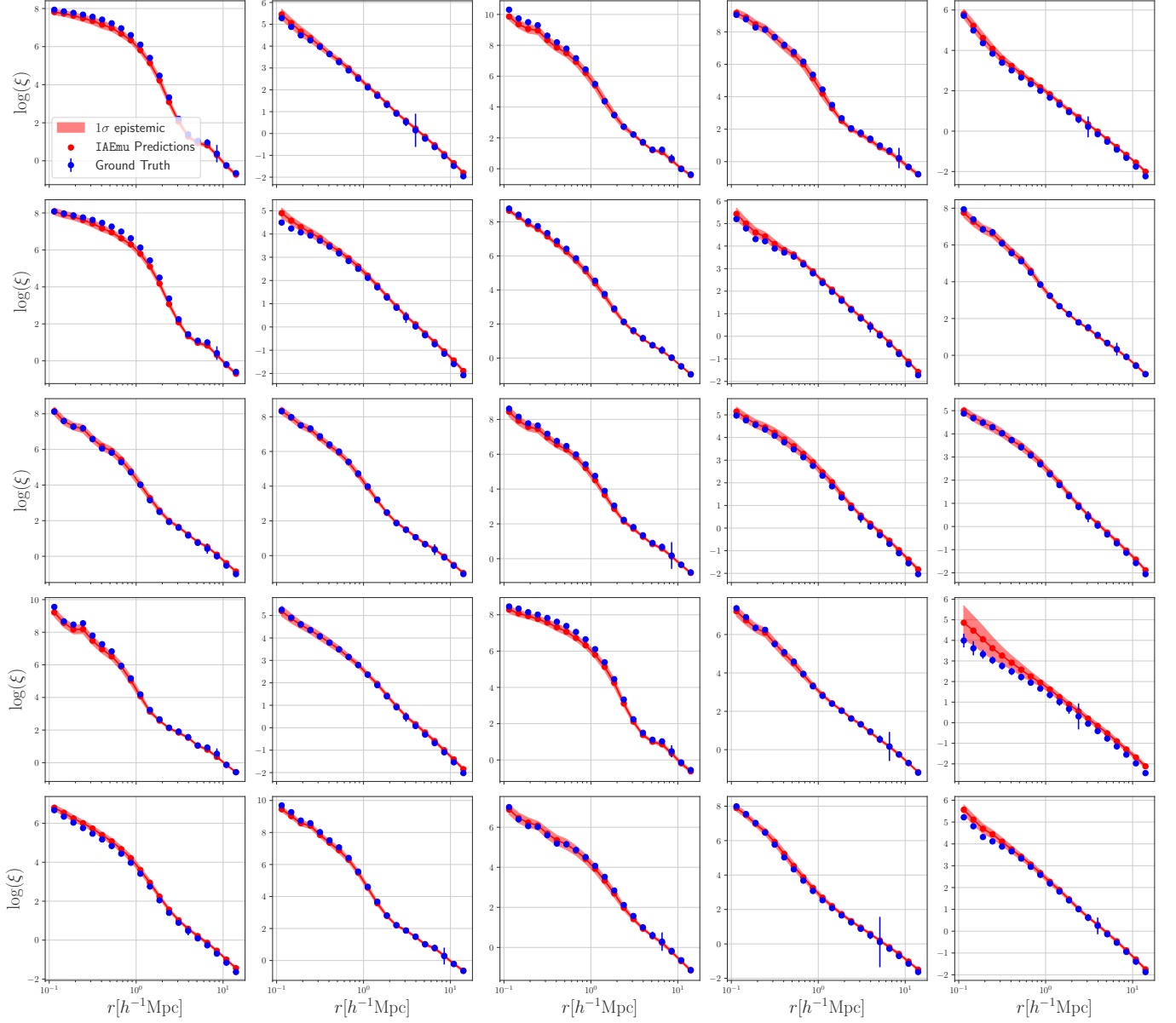


Figure D1. 25 random IAEmu test set predictions for ξ . $\log(\xi)$ is plotted due to the large range in correlation amplitudes. Error bars on ground truth values are computed across 10 realizations of `halotools-IA`. 1σ epistemic uncertainty is shown in the red shaded region.

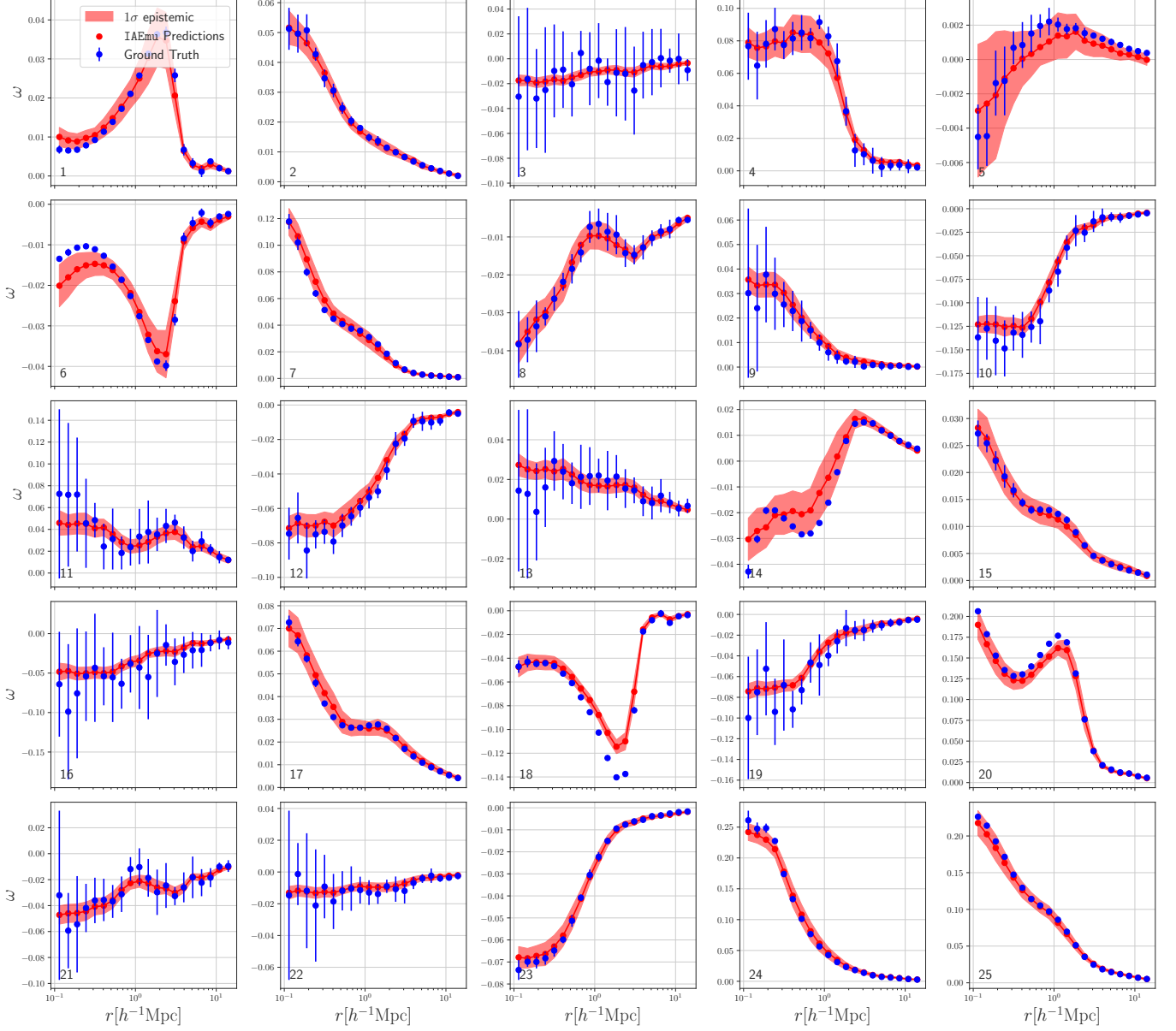


Figure D2. 25 random IAEmu test set predictions for ω . Error bars on ground truth values are computed across 10 realizations of `halotools-IA`. 1σ epistemic uncertainty is shown in the red shaded region.

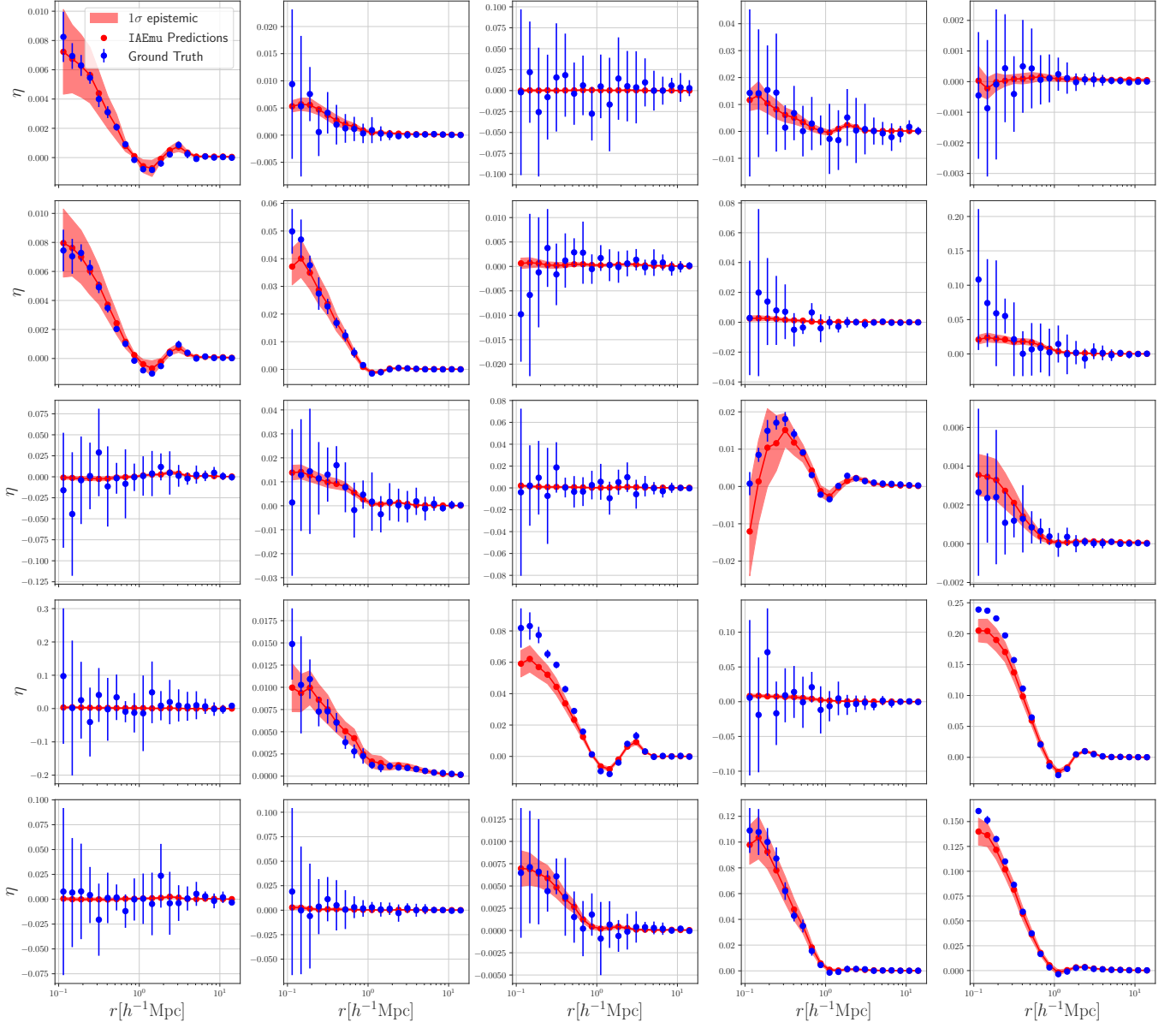


Figure D3. 25 random IAEmu test set predictions for η . Error bars on ground truth values are computed across 10 realizations of `halotools-IA`. 1σ epistemic uncertainty is shown in the red shaded region.